NTNU

Norwegian University of
Science and Technology

# Study of sediment erosion in guide vanes of Francis turbine

Lars Petter Nora

Master of Energy and Environmental Engineering
Submission date: June 2016
Supervisor: Ole Gunnar Dahlhaug, EPT
Co-supervisor: Biraj Singh Thapa, EPT
Sailesh Chitrakar, EPT

Norwegian University of Science and Technology
Department of Energy and Process Engineering

NTNU
Norwegian University
of Science and Technology

Department of Energy
and Process Engineering

EPT-M-2016-93

# MASTER THESIS

for

Lars Petter Nora

Spring 2016

***Study of sediment erosion in guide vanes of Francis turbine***

*Studier av sedimenter erosjon i ledeskovler av Francis turbin*

**Background**

Sediment erosion in Francis turbines is a large problem for river power plants near the Himalayas and the Andes Mountains. Due to high sediment concentration in the rivers the turbine components are exposed to erosion wear and must be maintained often. During monsoon periods, the sediment concentration is at its highest and the turbines are stopped to reduce the damage on the components. The turbines at Jhimruk Power Plant in Nepal are a good example on how the sediment erosion effects the power plant operation. These turbines need to be maintained annually due to high erosion wear. This result in a reduction of energy production and high maintenance cost. It is therefore of interest to have deeper knowledge of relation between flow behaviour and sediment erosion in these turbines. Cooperation between Kathmandu University and NTNU has started with an aim to develop Francis turbines that can withstand high sediment load.

**Objective**

The aim is to conduct numerical analysis and experimental investigation to identify effects of sediment erosion on guide vanes of Francis turbines

**The following tasks shall be considered in the project work:**

1. Literature survey
   a. Numerical analysis for sediment erosion

2. Software knowledge
   a. Get familiar with CFD-analysis with Ansys

3. Carry out CFD-analysis for the following cases:
   a. Symmetrical profile with and without clearance gap
   b. Asymmetrical profile with and without clearance gap
   c. Insert particles in all cases and analyse where the erosion will occur

4. Carry out experimental works on the asymmetrical profile
   a. Carry out pressure and velocity-measurements

5. Compare CFD-analysis with the experimental work

Within 14 days of receiving the written text on the master thesis, the candidate shall submit a research plan for his project to the department.

When the thesis is evaluated, emphasis is put on processing of the results, and that they are presented in tabular and/or graphic form in a clear manner, and that they are analyzed carefully.

The thesis should be formulated as a research report with summary both in English and Norwegian, conclusion, literature references, table of contents etc. During the preparation of the text, the candidate should make an effort to produce a well-structured and easily readable report. In order to ease the evaluation of the thesis, it is important that the cross-references are correct. In the making of the report, strong emphasis should be placed on both a thorough discussion of the results and an orderly presentation.

The candidate is requested to initiate and keep close contact with his/her academic supervisor(s) throughout the working period. The candidate must follow the rules and regulations of NTNU as well as passive directions given by the Department of Energy and Process Engineering.

Risk assessment of the candidate's work shall be carried out according to the department's procedures. The risk assessment must be documented and included as part of the final report. Events related to the candidate's work adversely affecting the health, safety or security, must be documented and included as part of the final report. If the documentation on risk assessment represents a large number of pages, the full version is to be submitted electronically to the supervisor and an excerpt is included in the report.

Pursuant to "Regulations concerning the supplementary provisions to the technology study program/Master of Science" at NTNU §20, the Department reserves the permission to utilize all the results and data for teaching and research purposes as well as in future publications.

The final report is to be submitted digitally in DAIM. An executive summary of the thesis including title, student's name, supervisor's name, year, department name, and NTNU's logo and name, shall be submitted to the department as a separate pdf file. Based on an agreement with the supervisor, the final report and other material and documents may be given to the supervisor in digital format.

☒ Work to be done in lab (Waterpower lab, Fluids engineering lab, Thermal engineering lab)
☐ Field work

Department of Energy and Process Engineering, 11th January 2016

Olav Bolland
Department Head

Ole Gunnar Dahlhaug
Academic Supervisor

Co-Supervisors:

- Torbjørn K. Nielsen
- Sailesh Chitrakar
- Biraj Singh Thapa

# Preface

This master thesis has been written at the Water Power Laboratory, under the Department of Energy and Process Engineering at NTNU. The thesis is a part of a research cooperation between NTNU and Kathmandu University to reduce sediment erosion in Francis turbine systems. The master thesis is a continuation of a Project thesis carried out during the fall of 2015 and will include some of the work done there.

It has been an interesting, fun and challenging year at the Water Power Laboratory. I have to thank my supervisor Ole Gunnar Dahlhaug and PhD students Sailesh Chitrakar and Biraj Singh Thapa. They have always had time to answer my questions and help me with my thesis. Our cooperation in carrying out the PIV experiments was invaluable and essential for me to be able to produce the results presented in this thesis.

I would also like to thank Carl Bergan, Peter Joachim Gogstad and Bjørn Solemslie for all the help they have provided. A special thanks goes to Bjørn Erik Rasmussen and Igor Iliev for all the good discussions and help they have given me with Ansys CFX. This has saved me several hours of extra work and increased my CFD knowledge a lot.

At last I must mention the fantastic environment that the Water Power Laboratory has provided. It has been a place for hard work, good discussions and lots of fun. I doubt my final year at NTNU could have been better anywhere else.

**Lars Petter Nora**
**Trondheim, June 10, 2016**

# Abstract

The Himalayas and the Andes mountains are regions with some of the worlds biggest hydropower potential. One of the biggest problems facing the development of these resources is high concentrations of hard minerals in the water streams. This causes severe sediment erosion in the hydraulic machinery. As a result, the maintenance cost is increased and the power production decreases.

With a goal to learn more about this problem, NTNU and Kathmandu University have initiated an large research cooperation. Together they have done a extensive research on a Francis turbine at the Jhiruk Hydroelectric Centre in Nepal, which operates with a high sediment load. As an extension of this research, a test rig designed as a symmetric section of this turbine has been made at the Water Power Laboratory at NTNU. The test rig, called the One GV Cascade, enables researchers and students to carry out experiments and study the passages flow conditions.

By carrying out a Computational Fluid Dynamics(CFD) and Particle Image Velocimetry(PIV) analysis on this test rig, one can study in detail the flow around different guide vanes(GV). Through comparing the CFD results with the experimental results, it is possible to evaluate in detail how the different GV geometries and clearance gap(CG) sizes will affect the flow. These results will hopefully make it possible to propose an improved GV design that causes less sediment erosion in the Francis turbine system.

This master thesis will describe the basic theory, procedures and results from the CFD and PIV comparison. The main results shows that the new GV design(NACA 4412) has much better flow conditions compared with the reference design(NACA 0012). The new GV design creates a lot smaller pressure difference between the suction and pressure side. The effect of this is also obvious with 15.7% lower clearance gap(CG) velocities, as well as a significantly smaller and weaker vortex filament.

To further confirm these results further studies has to be done. By designing a new test rig, with walls based on NACA 4412, the improved GV result can be further validated. If the same results are obtained, NACA 4412 can be seen as a promising improvement in the effort of removing one of hydropowers biggest

problems.

**Keywords:** Francis turbine, guide vane, sediment erosion, PIV, CFD.

# Sammendrag

Andesfjellene og Himalaya er fjellregioner med noen av verdens største potensialer for vannkraftsproduksjon. Et av de store hindrene for utbygging og utnyttelse av dette potensialet er høye konsentrasjoner av harde mineraler som kvarts og feltspat i elver og bekker. Dette øker vedlikeholdskostnadene betraktelig og senker kraftproduksjonen fra kraftverkene.

Med mål om å øke forståelsen av dette problemet har NTNU og Kathmandu University igangsatt et stort forskningssamarbeid. Sammen har de gjort et omfattende forskningsarbeid på en Francis turbin, som i dag kjøres med høye sediment konsentrasjoner på Jhirurk Hydroelectric Centre. Som en naturlig videreføring av dette arbeidet har det blitt designet en testrigg ved NTNUs Vannkraftslaboratorium, basert på en symmetrisk del av refereanseturbinen. Denne gir gode muligheter for forskere og studenter til å studere strømningen rundt ulike ledeskovel geometrier innsatt i test riggen.

Ved hjelp av Computational Fluid Dynamics(CFD) og Particle Image Velocimetry(PIV) analyser av test riggen, kan nye ledeskovel geometrier foreslås og studeres. Gjennom sammenligning av disse resultatene er det mulig å undersøke i detalj hvordan ledeskovelens geometri vil påvirke strømningen. Forhåpentligvis kan disse resultatene bidra i utviklingen av ledeskovler, som vil redusere erosjonen i francisturbiner.

Denne oppgaven vil presentere de grunnleggende teoriene bak PIV og CFD i tillegg til beskrivelser av prosedyrene brukt i eksperimentet og CFD modellen. Dette vil forhåpentligvis danne et godt grunnlag for leseren til å kunne forstå og vurdere de presenterte resultatene. Resultatene viser en klar forbedring av strømningsforholdene rundt den nye ledeskovelgeometrien(NACA 4412). Med en forbedret trykkfordeling, lavere hastigheter i gapet mellom vegg og ledeskovel og en svakere virvel fra dette gapet.

For å kunne videre bekrefte disse resultatene, burde nye forsøk gjennomføres i en ny test rig. Denne burde ha vegger basert på en turbin med NACA 4412 som ledeskovler. Kun da kan resultatene evalueres med større sikkerhet og ses på som en lovende løsning på ett av vannkraftens store problem.

# Contents

# List of Figures

# List of Tables

# Nomenclature

**Acronyms**

| | |
|---|---|
| $BL$ | Boundary layer |
| $CG$ | Clearance gap |
| $RANS$ | Reynolds averaged Navier Stokes equations |
| $SST$ | Shear Stress Transport |
| CFD | Computational Fluid Dynamics |
| LE | Leading edge |
| PIV | Particle Image Velocimetry |
| TE | Trailing edge |

**Greek Symbols**

| | | |
|---|---|---|
| $\delta$ | Boundary layer thickness | $m$ |
| $\epsilon$ | Turbulent dissipation | $m^2/s^3$ |
| $\mu$ | Dynamic viscosity | $kg/(s \cdot m)$ |
| $\rho$ | Density of the fluid | $kg/m^3$ |
| $\varepsilon$ | Fitness ratio | $-$ |

**Symbols**

| | | |
|---|---|---|
| $\nu_t$ | Turbulent viscosity | $m^2/s$ |
| $B$ | Inlet height | $m$ |
| $c$ | Particle concentration | $-$ |
| $D$ | Diameter | $m$ |
| $f(\alpha)$ | Impingement angle | $-$ |
| $g$ | Gravity | $m/s^2$ |

| | | |
|---|---|---|
| $H$ | Head | $m$ |
| $K$ | Constant | $-$ |
| $k$ | Turbulent kinetic energy | $m^2/s^2$ |
| $L$ | Length | $m$ |
| $P_a$ | Atmospheric pressure | $Pa$ |
| $Q$ | Flow rate | $m^3/s$ |
| $u$ | Velocity component | $m/s$ |
| $W$ | Erosion rate | $mm/year$ |
| $y^+$ | Dimensionless wall distance | - |
| $Z$ | Number of items | - |

**Subscripts**

| | |
|---|---|
| 1 | Refers to inlet length |
| $CF$ | Refers to the GV covering factor |
| $env$ | Refers to environmental constant |
| $GV$ | Refers to guide vane |
| $gvo$ | Refers to guide vane outlet |
| $i$ | Refers to a force or velocity in i'th direction |
| $m$ | Refers to meridional direction |
| $mat$ | Refers to material constant |
| $n$ | Refers to the net head |
| $u$ | Refers to peripheral direction |

# Chapter 1

# Introduction

Regions like the Andes mountains and the Himalayas have an enormous hydropower potential. Hydropower could become an important source of renewable energy for many developing countries. People in the Himalayas often rely on wood and fossil fuels for heating and electricity production. This has negative consequences as heavy air pollution and deforestation. The development of hydropower could potentially revolutionize the energy mix and reduce green house gas emissions for countries in these regions.

To make this possible, it is important for these countries to develop the knowledge needed to solve some of the problems domestically. With the help of countries that have extensive experience with hydropower development, countries like Nepal can overcome these problems and build their own hydroelectric industry. Norway, Germany and Switzerland are all countries with experience on how to develop and operate hydropower plants. Through cooperation and sharing of knowledge, the undeveloped countries can gain valuable knowledge on the flow in turbines, prevention of sediment erosion, optimal operation of the power plants and maximizing equipment lifetime.

This sharing of knowledge might be just what some of the countries in the Himalaya region need. These countries have faced severe problems with large concentration of sediments in the water streams. This causes severe sediment erosion on the hydraulic machinery. A close cooperation has been made between NTNU and Kathmandu University in Nepal with a goal of developing turbines that can withstand high sediment concentration in the water flow. This will hopefully strengthen the hydropower knowledge in Nepal and provide applicable solutions to the sediment erosion problem.

## 1.1 Objective

The aim of this thesis will be to carry out analytical CFD studies on a guide vane cascade and to analyse a new guide vane design that hopefully can reduce

the sediment erosion in guide vanes of Francis turbines. By also conducting experimental studies on the new guide vane design, the results from the CFD analysis can be further validated. The knowledge will create a foundation for the development of guide vanes that will reduce the sediment erosion in a Francis turbine system.

## 1.2 Outline

Chapter two will start by defining wear, erosive wear and how/where it affects the Francis turbine and the guide vanes. Chapter three and four will briefly describe the theory behind the PIV system, and guide vane theory. Chapter five will describe the basics behind the computational model for the One GV Cascade. Chapter 6 describes the experimental design and analysis, which will together with the previous chapters make a good foundation for the reader to understand the results, discussions and conclusions further on in the thesis.

# Chapter 2

# Wear

The term wear describes the mechanisms causing the deformation of solids or loss of materials. These can be categorised as thermal, chemical and mechanical. For the relevance of this project, only mechanical wear will be described more in detail. Mechanical wear is further classified in to three different types: cavitation, abrasive wear and erosive wear. Only abrasive and erosive wear is caused by particles in the water.

## 2.1 Abrasive wear

Abrasive wear can be categorised in to four different types as shown in figure 2.1. The difference between abrasive and erosive wear is the velocity direction of the particle. If the particle passes parallel over a surface, the wear is classified as abrasive and can be described more in detail as:[**Stachowiak and Batchelor**, **1993**]

1. **Cutting**
   When the hardness of the particles is higher than the surface, the particles will grind the surface and remove material.

2. **Fracture**
   Surface fracture happens when surfaces with ceramic coating are hit by particles as shown in fig. 2.1 b).

3. **Fatigue by repeated ploughing**
   If the surface is ductile, the particles may deform the surface. Repeated ploughing can also cause fatigue in the material.

4. **Grain pullout**
   Grain pullout occurs mainly when the surface material has a weak boundary

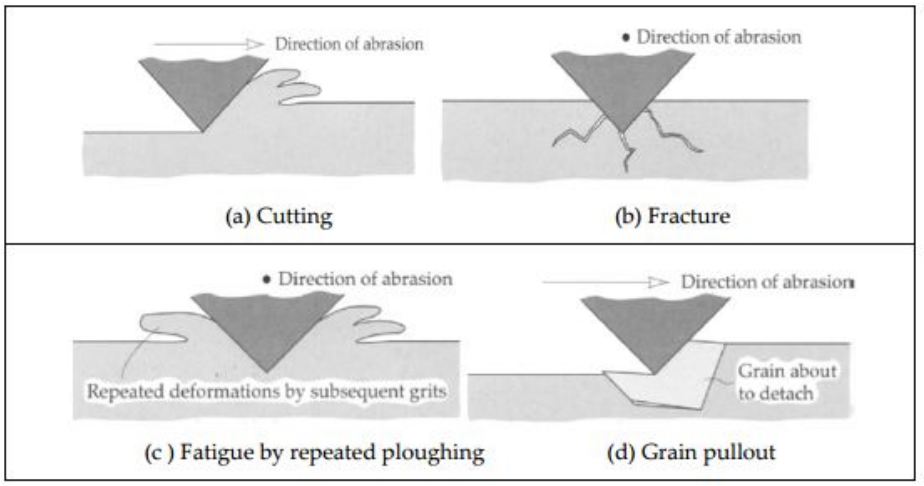


Figure 2.1: Types of abrasive wear. [**Stachowiak and Batchelor**, **1993**]

between grains. This typically happens to ceramic materials, where grains detaches and is transported further down the system by the water flow.

Relatively simple steps can be taken to prevent abrasive wear. By choosing a material for the hydraulic machinery with sufficient surface hardness, the wear is substantially reduced. This reduction in wear happens when the particle to material hardness ratio is under 1.2. [**Neopane**, **2010**]

## 2.2 Erosive wear

Erosive wear happens when the particles in the water impacts the hydraulic machinery. The rate of erosion is a function of the particles physical properties, its velocity, concentration in the water, flow pattern, the hydraulic machinery materials, etc.

Erosive wear from solid particles, can as abrasive wear, be defined in to four different mechanisms. Those are surface fatigue, brittle fracture, plastic deformation and cutting as shown in figure 2.2 and described in further detail as:

1. Surface fatigue
   After continuous hitting of the surface the particles create cracks and fatigue. This happens with particles that has low speed and large angle of impact. With time this will cause particles to detach from the surface.

2. Brittle fracture
   If particles hit the surface with medium velocity and large impingement

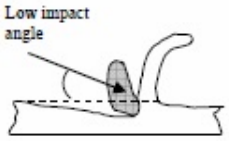


Figure 3.2.2: Cutting (abrasive) erosion mechanism

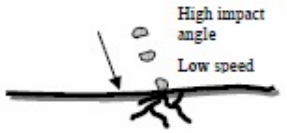


Figure 3.2.3: Fatigue erosion mechanism

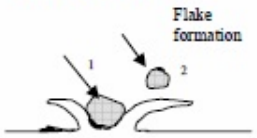


Figure 3.2.4: Plastic Deformation

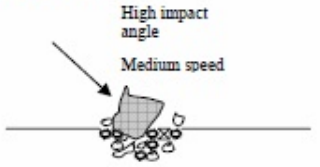


Figure 3.2.5: Erosion by brittle fracture

Figure 2.2: Types of erosive wear. [**Thapa**, **2004**]

angle, the particle can cause brittle fracture. This especially happens if the particles are sharp and will lead to detachment of particles due to sub surface cracking.

3. Plastic deformation
   Plastic deformation happens when particles hits the surface and creates flake formations at the point of impact. This happens at medium speed and a large impingement angle. After multiple strikes the flakes will detach as debris in to the water flow.

4. Cutting
   Particles with sharp edges that hits the surface with a low impingement angle will remove materials by scrapping or scouring the surface. This will form short track-length scars and is called cutting.

## 2.3 Erosion in Francis turbine

As seen in figure 2.3, the sediment erosion in Francis turbines occurs in areas where the velocities and/or the acceleration are the highest. In a turbine system the absolute velocities can reach up 70 m/s. This will potentially cause erosion in places like the stay vanes, guide vanes, and at the runner inlet and outlet. Only erosion at the guide vanes will be discussed in further detail.

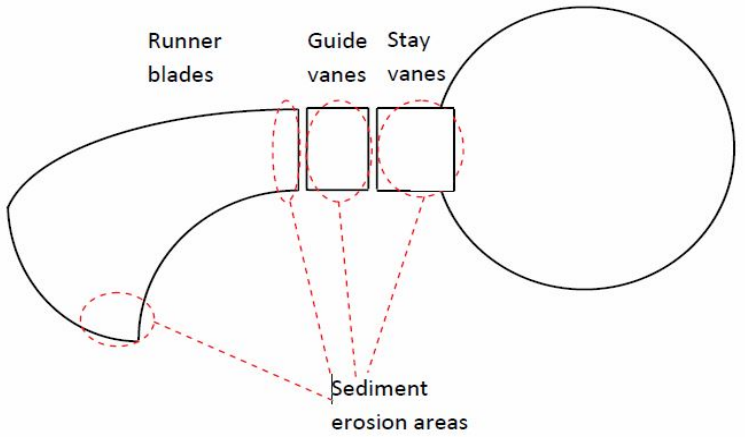


Figure 2.3: Areas heavily affected by sediment erosion. [**Gjosaeter 2011**]

### 2.3.1 Erosion in the guide vane system

Because of the waters high absolute velocity and acceleration the GV will be highly affected by sediment erosion. In a high head turbine the relative velocity head increases from about 0.1 to 0.5 from the GV inlet to the runner inlet. At full load and normal speed there will be a pressure drop across the guide vane at approx 40% of the net head(Hn). If this is changed to a small/closed opening the drop will be 50% of Hn.

The effects of this pressure drop causes erosion in the guide vane cascade. There are five different effects that causes erosion in the GV cascade. They are defined as [**Duan and Karelin**, **2002**]:

1. Turbulence erosion
   Occurs at the outlet of the GV and is mainly because of high velocity and fine grain sand. Also observed at the facing plates.

2. Secondary flow erosion
   Secondary flow erosion is the consequence of the creation of a horseshoe

vortex at the leading edge of the GV. The erosion is caused by fine grain and medium size sand, in the corners between the GV and the facing plates.

3. Leakage erosion
   The clearance gap between the guide vanes and the facing plates causes leakage flow from the pressure side to the suction side. The leakage increases the horseshoe vortex, local separation and the turbulence in the flow. It causes heavy erosion, from fine grain sand, at both the pressure side and the suction side.

4. Acceleration erosion
   The main flows acceleration also accelerates the particles in a normal direction to the guide vane surface and stream lines. This causes large grain particles to hit the GV surface and cause severe damage. The acceleration also creates secondary flow erosion in the corners of the GV and the facing plates.

Figure 2.4: Erosion in guide vanes [**Gjosaeter**, **2011**]

## 2.4 Models for erosion

There are several simplified erosion models that express the erosion rate as a function of the velocity and the material properties of the particles. Based on test results from wear tests, a normal expression for the erosion rate is:

$$Erosion \propto Velocity^i \tag{2.1}$$

The $i$ has often got a value close to three and is dependent on the material properties.

There is also a proportionality between erosion and the concentration of particles in the water. This is valid up to a certain limit where the particles hitting the "wall" and the ones bouncing off the wall will hit each other and lower the erosion rate. This can be written as:

$$Erosion \propto Concentration^k \tag{2.2}$$

Depending on the material, the $k$ varies from 0.25 and 1.27. Since the $k$ is often close to one, it is a valid approximation to evaluate the erosion as proportional to the concentration.

In total, the erosion rate is a function of multiple variables as operating conditions, surface material properties, and particle properties as seen in equation 2.3:

$$W = K_{mat} \cdot K_{env} \cdot c \cdot V^i \cdot f(\alpha) \qquad [mm/year] \tag{2.3}$$

$W$, is the erosion rate, the $K_{mat}$ is the material constant, $K_{env}$ is a constant describing the environment, while the concentration of particles is given by $c$, the $V^i$ is the same as described earlier and the impingement angle is given by $f(\alpha)$. There are also several other erosion models which takes in to account several more variables.[**Gogstad**, **2012**]

## 2.5 Measures to decrease erosion in Francis turbines

As a result of the reduction in the thickness of the hub, shroud and runner blades to increase the efficiency and the fact that material strengths have been unchanged, the system will be more vulnerable to erosive wear. There are several measures that can be made to counteract this. Some of these measures are presented in table 2.1.

A detailed cost analysis has to be done to evaluate whether the investments will be worth it when the total gain is weighed against the cost of the measures. There might also be other challenges that will make it difficult to apply these measures. Since coating always must be applied after the turbine is assembled, it is difficult

Table 2.1: Measures to prevent sediment erosion[**IEC**, **2012**]

| Measure | Advantage | Disadvantage |
|---|---|---|
| Coating on exposed parts | Increasing the resistance against abrasion of the surface | Surface roughness might be increased, which will increase production cost and might lower the efficiency. |
| Thicker runner blades | Increasing the time before the erosive damages significantly affects the efficiency | The risk of vibrations from von Karman vortices are increased and the efficiency decreases |
| Increase the diameter of the turbine | Erosion is reduced by reducing the relative velocity | Increased requirements for space and material costs |
| Reducing number of runner blades | Increasing access of the flow channel for coating purposes | Might increase cavitation in the runner |

to apply coating on smaller turbines. In 2010, scientist at NTNU managed to manufacture a turbine without using welding. This allowed smaller turbines to be coated before assembly, and still have optimal performance. [**Dynavec**]

# Chapter 3

# Particle Image Velocimetry

A optical method often used in research and education to visualize flow is Particle Image Velocimetry. By inserting tracer particles in to the fluid and illuminating them, the particles works as instant markers for the fluid motion. With the help of high resolution cameras and software, it is possible to create accurate 2D and 3D vector fields by tracking particles from one picture to another. The main fundamentals will be discussed briefly in this chapter and in more detail in the Appendix.

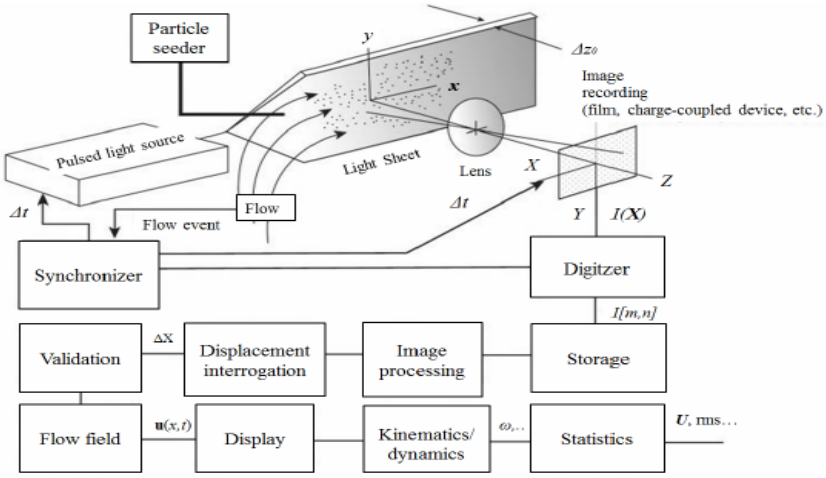


Figure 3.1: Main components and processes of a PIV system. [**Adrian & Westerweel**, **2011**]

**Basic theory**
In the standard 2D PIV system, the laser creates a thin laser sheet which illuminates the particles in the plane. By capturing images at time $t = t_0$ and at $t = t_0 + \Delta t$ the particles are tracked in groups or by individual movement. To ensure a minimum deviation between the movement of the particles and the

fluid, the type of particles must be carefully selected. Important features are the density, size and light scattering properties. The most important components and processes in the PIV can be seen in figure 3.1.

As seen in figure 3.1, the software will create a coordinate system in the light sheet(x,y) and accordingly in the image frame(X,Y).The Z is the distance from the camera to the illuminated plane. To create a relationship between the (x,y) position in the illuminated sheet and the (X,Y) position in the image frame, the target plane is calibrated. Further information on the calibration, PIV theory and processes can be found in Appendix F.

# Chapter 4

# Foil Theory

To create a new guide vane design that will reduce the effects of sediment erosion, it is important to follow the general rules of GV design and optimum flow conditions. It's only through combining these rules and knowledge gained on sediment erosion, that it is possible to develop the optimal design. A design that both creates the best flow conditions and erosion resistance.

## 4.1 Flow around GV

A guide vanes purpose is to change the direction of the water and to optimize the flow direction in to the runner. This sudden change of the water flow angle can cause a significant pressure difference on the two sides of the guide vane. This pressure difference will cause higher velocities at the side with the lowest pressure(suction side) and lower velocities at the side with higher pressure(pressure side). The flows governing equations can be expressed as:

$$\frac{\partial u}{\partial x} + \frac{\partial v}{\partial y} + \frac{\partial w}{\partial z} = 0 \tag{4.1}$$

$$\rho \cdot \frac{Du_i}{Dt} = -\frac{\partial p}{\partial x_i} + \rho \cdot g_i + \mu \cdot (\frac{\partial^2 u_i}{\partial x^2} + \frac{\partial^2 u_i}{\partial y^2} + \frac{\partial^2 u_i}{\partial z^2}) \tag{4.2}$$

The wake behind the guide vanes is formed by the tripped boundary layers on the GV body. This boundary layer(BL) is dependent on the shape of the GV, its angle of attack and the velocity of the flow. As a result of adverse pressure gradient and insufficient momentum exchange, the boundary layer will separate from the GV body.

This separation creates a wake that will both disturb and change the flow further downstream of the GV. If the Reynolds number is increased and the BL becomes turbulent, it will separate at a later point. This will create a smaller wake and as a result of this, smaller disturbances in the water flow towards the runner.

**Clearance gap flow**
The pressure difference between the two sides of the GV is one of the main focuses in this thesis. This pressure difference will also be the reason for a leakage flow in the gap between the GV and the facing plates of the wicket gate. The flow which will be driven from the pressure side to the suction side will carry sediments and cause erosion damages in the clearance gap. This flow in the clearance gap, as seen in figure 4.1, will cause a local separation of the BL and increase the turbulence at the suction side of the GV.

This leakage flow also creates a filament vortex seen in figure 4.1. This vortex will continue downstream and cause heavy erosion at the runner inlet. As time goes by and sediment erosion increases the size of the clearance gap, the leakage flow increases the filament vortex. This vortex will increasingly disturb the flow and change its direction towards the runner inlet. This does not only increase the erosion, but will also gradually decrease the power output.

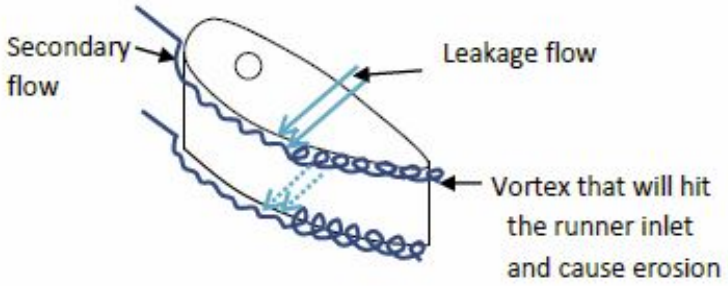


Figure 4.1: The creation of filament vortex [**Gjosaeter**]

By studying the governing equations more in detail, it is possible to get a more solid understanding of why the clearance gap flow appears. Based on the elementary lubrication theory, the momentum equation for flow in a confined space can be expressed as in equation 4.3. This equation is based on a 2D flow in x direction, along a narrow passage with height h. The equation can then be expressed as:

$$\rho \cdot (\frac{\partial u}{\partial t} + u \cdot \frac{\partial u}{\partial x} + v \cdot \frac{\partial u}{\partial y}) = -\frac{\partial p}{\partial x} + \rho \cdot g_x + \mu \cdot (\frac{\partial^2 u}{\partial x^2} + \frac{\partial^2 u}{\partial y^2}) \qquad (4.3)$$

By applying order of magnitude and inserting dimensionless variables, it is easier to evaluate which of the terms can be neglected and which are important. These dimensionless variables are defined as:

$$y^* = \frac{y}{h} = \frac{y}{\varepsilon \cdot L}, x^* = \frac{x}{L}, u^* = \frac{u}{U}, v^* = \frac{v}{\varepsilon \cdot U}, t^* = \frac{U \cdot t}{L}, p^* = \frac{P}{P_a}, \varepsilon = \frac{h}{L} \quad (4.4)$$

$\varepsilon$ expresses the passages fitness ratio, the flows characteristic velocity is defined by U, and $P_a$ is the atmospheric pressure. By applying order of magnitude, equation 4.3 can be expressed as:

$$x : 0 \cong \frac{-1}{\rho} \cdot \frac{\partial p}{\partial x} + \frac{\partial^2 u}{\partial y^2}, \qquad y : 0 \cong \frac{-1}{\rho} \cdot \frac{\partial p}{\partial y} \tag{4.5}$$

Integrating these equations, gives the velocity u(x,y,t). Another equation that is important to define is the boundary layer thickness. This can be expressed through the Prandtl-Blausius boundary layer solution:

$$\delta_{lam} \approx \frac{4.91 \cdot x}{\sqrt{Re_x}} \qquad [m] \tag{4.6}$$

$$\delta_{turb} \approx \frac{0.382 \cdot x}{Re_x^{1/5}} \qquad [m] \tag{4.7}$$

## 4.2 General GV design rules

The guide vanes governs the discharge of water, as well as the waters angle entering in to the runner. When the runner vanes passes the guide vanes, pressure pulsation will occur. To minimize these pressure pulsations, the number of GV's has to follow the rule from equation 4.8.

$$\frac{Number\ of\ Guide\ vanes}{Number\ of\ Runner\ vanes} \neq Integer \tag{4.8}$$

It is a common design rule that the outlet diameter of the guide vane to be 5% larger than the runner inlet diameter. This gives acceptable distance between the runner and the guide vanes at rated power. At full power the gap between the runner inlet and GV outlet is less. It is also important to control that there is an acceptable clearance distance with this GV angle.

The free vortex theory can be used to find the absolute velocities tangential component at the guide vanes trailing edge.

$$C_{u1} r_1 = C_{uGVO} \cdot r_{GVO} = Constant \tag{4.9}$$

By using the continuity equation, with variables as the inlet height and the guide vanes inlet diameter, the meridional velocity component can be calculated through equation 4.10:

$$Q = A \cdot c_{mInletGV} = \pi \cdot D_1 \cdot B \cdot c_{mInletGV} \rightarrow c_{mInletGV} = \frac{Q}{\pi \cdot D_{inletGV} \cdot B} \qquad [m/s] \tag{4.10}$$

The meridional component can further be used to find the outlet angle of the guide vane:

$$tan\alpha_{gvo} = \frac{c_{mgvo}}{c_{ugvo}} \qquad [-] \tag{4.11}$$

After this, other important dimensions as the radial position $r_0$, $L_0$, and the total length of the guide vane as shown in figure 4.2a must be found. If the $r_0$ is known the law of cosine can be applied to find $L_0$.

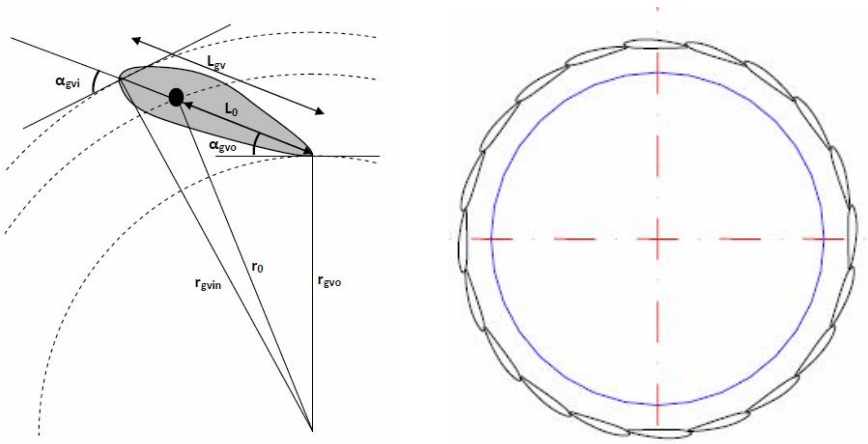


(a) Guide vane main dimensions. (b) Overlapping of the guide vanes

Figure 4.2: [**Gjoseater 2011**]

Depending on the number of guide vanes, the length $L_{gv}$ has to be sufficient to make the guide vanes overlap in the closed position as shown in figure 4.2b. To ensure that the guide vanes don't rotate further than the closed position, they have to overlap with a cover factor which makes is impossible for the GV's to rotate a whole circle. This cover factor is about 10 to 15% and is called $K_{cf}$. The total length can be calculated through equation 4.12

$$L_{gv} = \frac{\pi \cdot D_0 \cdot K_{cf}}{Z_{gv}} \qquad [m] \tag{4.12}$$

As seen in fig 4.2a, the GV axis should be placed in between 0.5 and 0.75 of the length from the trailing edge. The placement of the axis should fulfill the axis and overlap criterias. The law of cosine can once again be used to find the GV

inlet diameter. [**Gjosaeter 2011**]

NACA airfoil geometries are often used as guide vanes in Francis turbines. It is also NACA profiles that will be tested as GV geometries in this thesis. Further theory and basic concepts around the NACA profiles can be found in appendix A.

# Chapter 5

# Computational Fluid Dynamics

Calculation and experimentation are the two fundamental approaches of solving and analysing fluid flow engineering systems. With the help of computers, it is possible to computationally solve the equations of fluid flow (CFD). These CFD methods can produce detailed information about a fluid flow pressure, velocity, shear stress, etc.

Ansys CFX was chosen as the software to simulate the fluid flow. The reason for this choice was that NTNU has bought several licenses, and students have access to several Ansys resources. Also a large "in-house" experience with Ansys CFX, along with its ability to run flow simulations with sediments in the flow played a role.

## 5.1 Turbulence models

CFD can handle laminar fluid flow systems with great accuracy. If, on the other hand, the flow is turbulent, the CFD software will struggle to produce accurate solutions. To solve these problems, the CFD software will have to use turbulence models to solve the governing equations.

To solve the governing equations some of the turbulence models decompose time varying quantities in to time averaged quantities. This will simplify the governing equations and create the Reynolds averaged Navier Stokes equations (RANS).

The most common turbulence models are the two model equation models. These models tries to predict turbulence by solving two partial differential equations for two variables.

**k-$\epsilon$**
This model is a two-equation model which solves the transport equations for the turbulent kinetic energy k, and the turbulent dissipation $\epsilon$. This model will give the best results at free-shear layer flows with small or no adverse pressure gradients.

While solving the equations for these variables it is possible to define three new variables, L($= k^{3/2}/\epsilon$), $\tau(= k/\epsilon)$ and $\nu_t(= C_u \cdot k^2/\epsilon)$. L and $\tau$ is respectively a length and time scale and $\nu_t$ is the turbulent viscosity. Further information of the constants and variables can be found in [**Pope**].

$$\frac{Dk}{Dt} \approx \frac{\partial}{\partial x_i} \cdot \left( \frac{\nu_t}{\sigma_k} \cdot \frac{\partial k}{\partial x_i} \right) + \nu_t \cdot \left( \frac{\partial \bar{u}_i}{\partial x_j} + \frac{\partial \bar{u}_j}{\partial x_i} \right) \cdot \frac{\partial \bar{u}_i}{\partial x_j} - \epsilon \tag{5.1}$$

$$\frac{D\varepsilon}{Dt} \approx \frac{\partial}{\partial x_i} \cdot \left( \frac{\nu_t}{\sigma_\epsilon} \cdot \frac{\partial \varepsilon}{\partial x_i} \right) + c_v \cdot \frac{\varepsilon}{k} \cdot \nu_t \cdot \left( \frac{\partial \bar{u}_i}{\partial x_j} + \frac{\partial \bar{u}_j}{\partial x_i} \right) \cdot \frac{\partial \bar{u}_i}{\partial x_j} - c_2 \cdot \frac{\varepsilon^2}{k} \tag{5.2}$$

$$\nu_t \approx \frac{C_\mu \cdot k^2}{\varepsilon} \tag{5.3}$$

**k-$\omega$**
This is another two equation RANS model. It uses two partial differential equations for the turbulent kinetic energy, k, and the specific turbulence dissipation rate, $\omega$, to predict the turbulence in the flow. Unlike the k-$\epsilon$ model, this model performs better/best in areas of transitional flow and adverse pressure gradients. The model will therefore also be sensitive to free stream values and it is important to evaluate the $y^+$(dimensionless wall distance) value in non turbulent free stream boundary.

The last transport equation and the turbulent viscosity can be written as:

$$\frac{D\omega}{Dt} \approx \frac{\partial}{\partial x_i} \cdot \left( \frac{\nu_t}{\sigma_\omega} \cdot \frac{\partial \omega}{\partial x_i} \right) + c_v \cdot \frac{\omega}{k} \cdot \nu_t \cdot \left( \frac{\partial \bar{u}_i}{\partial x_j} + \frac{\partial \bar{u}_j}{\partial x_i} \right) \cdot \frac{\partial \bar{u}_i}{\partial x_j} - c_2 \cdot \frac{\omega^2}{k} \tag{5.4}$$

$$\nu_T \approx \frac{C_\mu \cdot k^2}{\omega} \tag{5.5}$$

**k - $\omega$ SST**
To get a turbulence model that combines the k-$\epsilon$ accuracy in free stream flow and the strengths of the k - $\omega$ model at viscous sub layers, the k-$\omega$ SST is the best option. To get a good solution in the transition area, seen in figure 5.1, the function uses a blending function of the two in turbulence models.

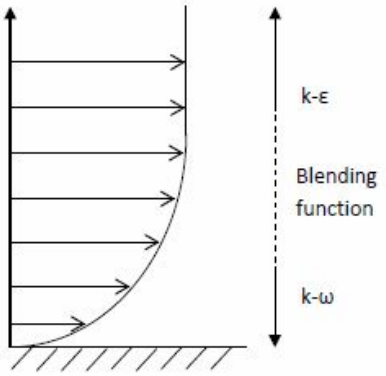


Figure 5.1: SST model [**Gjosaeter 2011**]

## 5.2 Grid specification

To produce accurate CFD results it is important to have a well defined grid. The quality of the grid will also affect the convergence of the solution. The quality is often measured through the aspect ratio, skewness and mesh orthogonality.

To define the mesh resolution, it's normal to use the previously mentioned variable called $y^+$. The variable defines the distance from the wall to the nearest mesh node. The $y^+$ is defined as:

$$y^+ = \frac{\rho \cdot \Delta y \cdot u_t}{\mu} \qquad [-] \tag{5.6}$$

$\Delta y$ is the distance from the wall to the first mesh node in meters, the friction velocity $u_\tau$, is given by equation 5.7

$$u_\tau = (\frac{\tau_\omega}{\rho})^{1/2} \qquad [m/s] \tag{5.7}$$

The $\tau_\omega$ represents the wall shear stress.

Multiple turbulence models have spesific requirements for $y^+$. The required mesh resolution for the $k-\omega$ SST model is $y^+ \approx 1$. This ensures an accurate solution for the flow within the viscous sub layer. Such a low $y^+$ can be hard to achieve and will have great computational cost. [**Thapa 2012**]

An alternative to this method is to simplify the computation by not completely resolving the near wall flow. Instead it is possible to use a wall function which uses empirical formulas with appropriate values for the velocity profiles close to the wall, as shown in figure 5.2

Extensive recearch has been done on the quality of the results with the deacreased mesh resolution. To get acceptable results, Apsley reccomends a $y^+$ between 30 to 150. Because of simmilar arguments in B.S. Thapas's master thesis and other papers, $y^+$ values from 20 to 100 in the area of interest will be considered as acceptable in this thesis. [**Thapa 2012**]

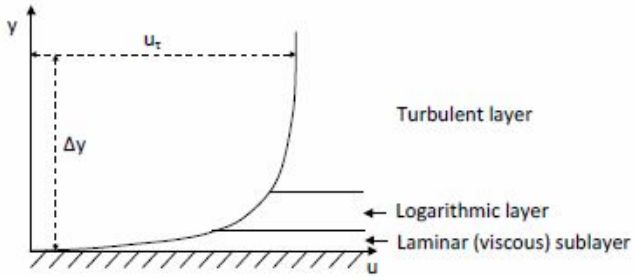


Figure 5.2: Wall function [**Thapa 2012**]

**Mesh independency**
To ensure a correct solution, it has got to be independent of the mesh. By testing the solutions with a "mesh independency test," one can assure that the mesh meets the criterias. These are:[**Dahl 2014**]

- The residual RMS values has reached acceptable low values, often in the range of $10^{-4}$ or $10^{-5}$.
- Steady state solution. The monitoring points must have converged to a steady state value.
- A imbalance in the domain of less than 1% of the variables.

If the solution does not change with different meshes and the criteria above are met, the solution is mesh independent. By checking multiple types of mesh, it is possible to choose the coarsest of the independent meshes. This will save computational time.

**Boundary conditions**
Before running simulations, one has to define boundary conditions and flow parameters in Ansys CFX-Pre. Is the flow viscous or inviscid, what can be defined as walls and what areas are inlets/outlets. If the flow is viscous, a no slip condition has to be set at the walls.

**Erosion models**
CFD modelling provides detailed info on both the placement and the magnitude of the erosion. For this thesis, only single phase CFD simulations will be relevant.

CFD software as ANSYS can provide several models for erosion. The methology is based on the Eulerian and Lagrangian flow field theory. In Ansys CFX there are two different erosion models. These are the Tabakoff and Grant erosion model and the Finnie's erosion model. Further information can be found in B. Thapas PhD, for sediment erosion simulation. [**Thapa 2004**]

# Chapter 6

# Computational model for One GV Cascade

Ansys 15.0 has been used to do the numerical modelling, the meshing and simulations of the test rig referred to as One GV Cascade. The geometry, seen in figure 6.1, has been created in Creo Parametric and imported in to Ansys.

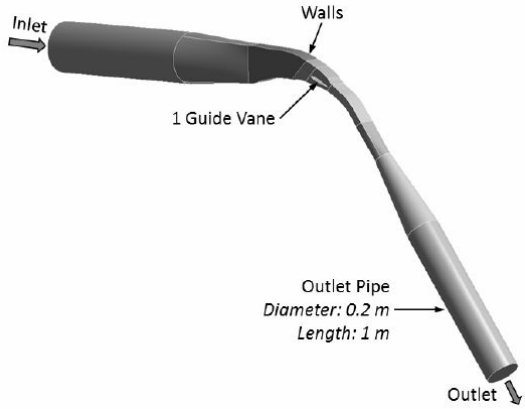


Figure 6.1: Imported CAD geometry of the test rig [**Thapa**, **2016**]

The mesh was generated through Ansys meshing. The geometry was pieced in to multiple parts as seen in fig 6.2. This made it possible to apply different densities according to the parts which are most important and are areas of interest. These are especially the areas around the GV and directly after the GV. By combining a fine mesh, with thin inflation layers, it is hopefully possible to capture the fluid flow where the velocity is highest.

The body sizing method was used to control the size of the elements in each part of the test rig. The walls of the test rig was set as a smooth, no slip wall. The

inlet condition was given by a normal speed of 0.46 m/s, and the outlet condition by an average static pressure of 303 kPa.

**Mesh independency**

To check the quality of the mesh, a mesh independency test was done with a k-$\epsilon$ turbulence model on the NACA 0012 profile. The test consisted of 6 different meshes with varying density from 0.2 to 10 million cells. The test was done by gradually refining the grid resolution of the inflation layers and in the boxes showed in figure 6.2

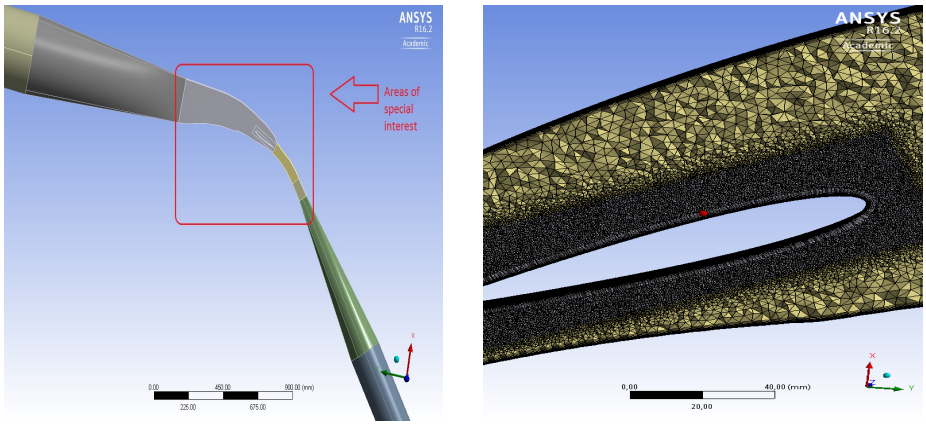


Figure 6.2: Meshing sections of test rig and GV generated mesh

The result of the mesh independency test can be seen in figure 6.3. Where the $C_u$ velocities at the runner inlet line has been plotted for each mesh. As seen in figure 6.3 the results vary a lot, especially between 0.2 mill nodes and the higher ones.

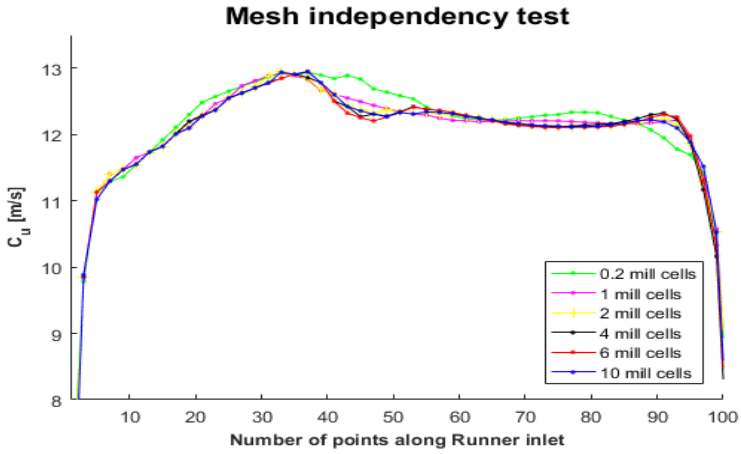


Figure 6.3: Mesh independency test

The best and most stable results can be seen from the meshes with 2, 4, 6 and 10 million nodes. From these results it is obvious that the meshes with the highest density most clearly highlights the effects of the GV wake. 4 million nodes seems sufficient for the analysis, but the 6 million will be used to ensure an high accuracy of the results.

Several other studies has previously done mesh independency tests on the One GV Cascade test rig. By comparing these results with previously done mesh independency test, the same trends are obvious. Even though these studies have used a structured mesh with better mesh control, the results are the same. On this basis, it is possible to say that this mesh will be suficcient for simulating the flow around the two GV profiles. [**Thapa**, **Trivedi & Dahlhaug**]

**Turbulence test**
Another tool to investigate the fow around the GV is a turbulence test. Six different turbulence models was tested, these were $k-\epsilon$, $k-\epsilon$ RNG, $k-\omega$, $k-\omega$ SST, $k-\omega$ reynolds stresses, and eddy viscosity. The theory behind these models will not be discuessed further in this paper, but extensive information can be found in [**Versteeg & Malalaseker**].

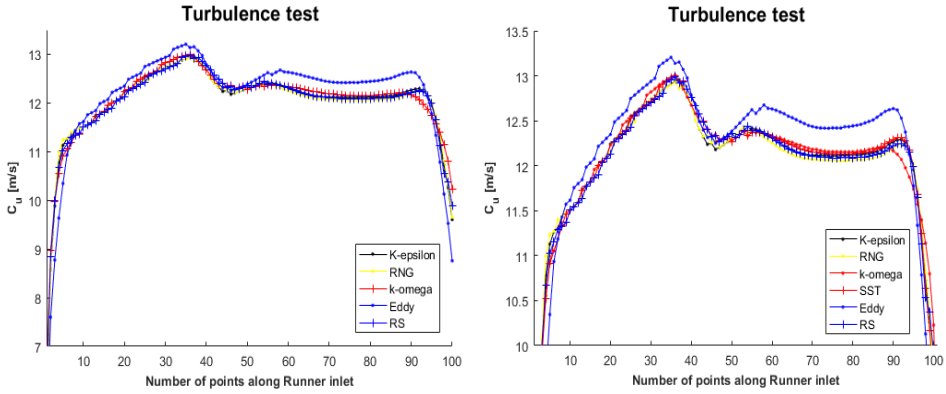


Figure 6.4: Results of turbulence test

Presented in fig 6.4, the results are compared by the $C_u$ velocities at the runner inlet line. Even though the results show the same trends, the results of the different turbulence models vary considerably. This is especially at higher velocities, seen in the velocity plot. The eddy viscosity model shows the highest velocities of the models and lie substantially over the rest in the plot. At the edge, k-omega drops earlier than the other models close to the wall. This could be because of too few inflation layers within the laminar part of the BL. All of the models are able to give results that indicate a clear GV wake.

After consultation with PhD students and comparing with previous turbulence tests done for the One GV Cascade, the results from the k-$\epsilon$ was considered good

enough. The final properties of the mesh and the simulation can be found in Appendix B. [**Thapa**, **Trivedi & Dahlhaug**].

# Chapter 7

# Experimental design and analysis

## 7.1 Design of flow cascade

**Reference design**
Being able to carry out experiments and study the effects of sediment erosion in a Francis turbine, the flow conditions in the One GV Cascade needed to be similar to the flow in an actual turbine. The test section is therefore designed as a symmetric section of a reference turbine in the Jhimruk Hydroelectric Centre in Nepal. This turbine was chosen because it normally operates with high sediment load and it is therefore interesting to replace it with a more erosion resistant turbine.

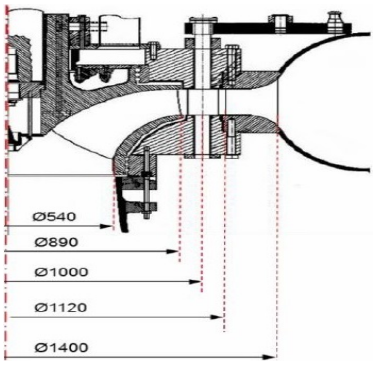


| Parameters | Symbol | Unit | Value |
|---|---|---|---|
| Net head | H | m | 201.5 |
| Flow rate per unit turbine | Q | m3/s | 2.35 |
| Rotational speed | n | rpm | 1000 |
| Speed number | Ω | - | 0.32 |
| Number of blades in runner | Z_Blades | # | 17 |
| Inlet diameter of runner | D_1 | m | 0.89 |
| Outlet diameter of runner | D_2 | m | 0.54 |
| Number of Guide vanes | Z_gv | # | 24 |
| Chord length of GV | L_gv | m | 0.14 |
| Profile of GV surface | - | - | NACA-0012 |

Figure 7.1: Turbine dimensions and analytical design values [**Thapa**, **Trivedi & Dahlhaug**]

Previously there has been done extensive research on the design of the turbine to maintain the efficiency while reducing the erosion. This has been done with the help of an analytical design software called "Khoj". With this research as

background it was a natural extension to study the erosion in the guide vanes and its effect on the flow to the runner inlet blades. Some relevant information about the reference turbine is given above.

**Design of One GV Cascade**
For the One GV Cascade, three guide vanes has been chosen to form the test rig. These three guide vanes forms 2 out of a total of 24 flow passages in the guide vane section of the turbine. The walls are "defined" by the outer guide vanes. This is to reduce the effects of the walls on the flow around the center guide vane.

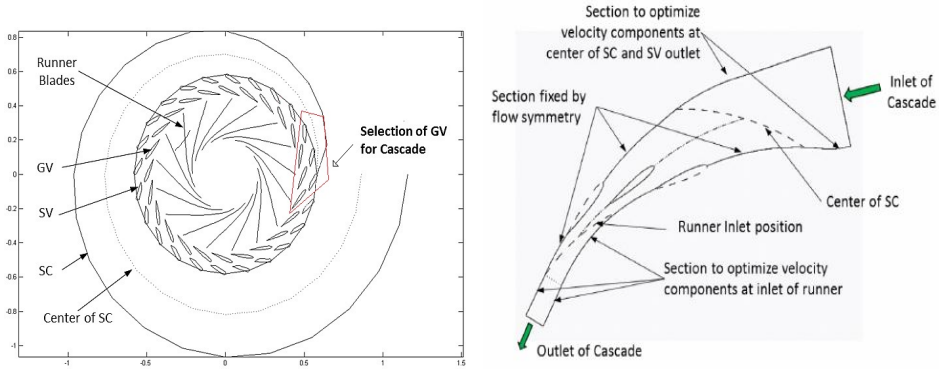


(a) Chosen turbine section (b) Wall profile for cascade flow

Figure 7.2: Development of One GV Cascade[**Thapa**, **Trivedi & Dahlhaug**]

The three chosen guide vanes that has been used to develop the test rig can be seen in figure 7.2a. By choosing the guide vanes at the end of the spiral casing a minimal size of the test rig is ensured. The wall profile of the cascade flow is seen in figure 7.2b, where the walls are defined from the spiral casing center, along the guide vanes and to the middle of the runner blade. To ensure correct inlet conditions of the flow, the test rig has been designed to give the correct/same velocity conditions(radial and tangential) from the centre of the spiral casing.

Other simplifications have also been made in the design of the test rig. There are no stay vanes and flat plates has replaced the circular portion of the spiral casing. The flat plates have the same height as the GV span. These simplifications will affect the flow conditions, but by normalizing the design, satisfactory flow conditions can be obtained.

**One GV Cascade setup**
The test section has been designed to measure the change in velocity and pressure distribution around the inserted GV. As shown in the figure 7.3, the test section is built with a plexiglass section. This makes it possible for a laser to illuminate the flow through the lower cover. A camera is used to take pictures of the illuminated flow through the front cover of the test rig.

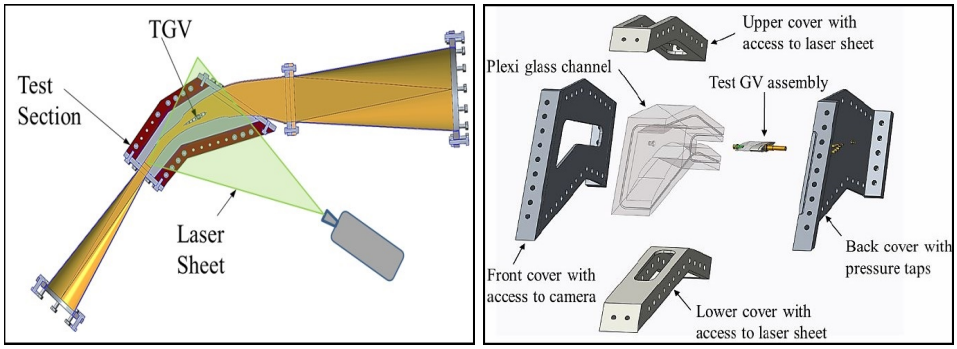


Figure 7.3: Test rig and exploded view of test section [**Thapa**, **2015**]

The test section is made out of multiple parts. These can be quite easily removed by loosening the bolts on the back and front cover as seen in figure 7.3. This allows the persons operating the test rig to efficiently do the experiments, take the test rig apart, and insert a new guide vane.

**Guide vane design**
The initial experimental design of the reference guide vane was made to fulfil the possibility to make both pressure and velocity measurements. As partially shown in figure 7.5, the first designs used in initial experiments made it possible to carry out PIV and pressure measurements around the GV and in the clearance gap.

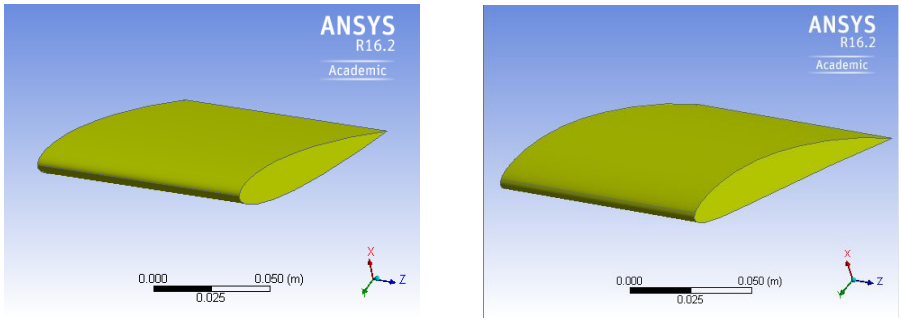


(a) Original design: NACA 0012 (b) New design: NACA 4412

Figure 7.4: Guide vane design

After multiple PIV experiments on the initial design shown in fig 7.4a, multiple CFD analysis was made to find another GV design that could reduce the erosion. By simulating flow in the test rig with several different NACA profiles, NACA 4412(fig 7.4b) showed the most promising results. The results showed a decrease in the pressure difference on the GV sides and smaller clearance gap flow. To further investigate and validate the CFD results, an experimental PIV study of the initial GV design and the improved design(NACA 4412) would be completed

in the test rig.

Because of the design of the test rig and the GV, there will be some parts that will "receive" less laser light than others. The bends at the edges of the GV, as well as bends at the wall of the test section, will cause optical distortions in the plexiglass. This prevents some of the light to hit the particles and will make it harder for the software to measure realistic velocities.

## 7.2 Pressure measurements

To measure the pressure in the flow, there were several taps for pressure measurements. As seen in figure 7.5, these were placed at important places in the test section to measure the pressure variation in the flow and around the GV. Some of these pressure taps was placed along the facing plates towards the leakage flow and others along the GV mid span surface at the middle part. This made it possible to measure and compare pressure values around the GV in the CFD results.

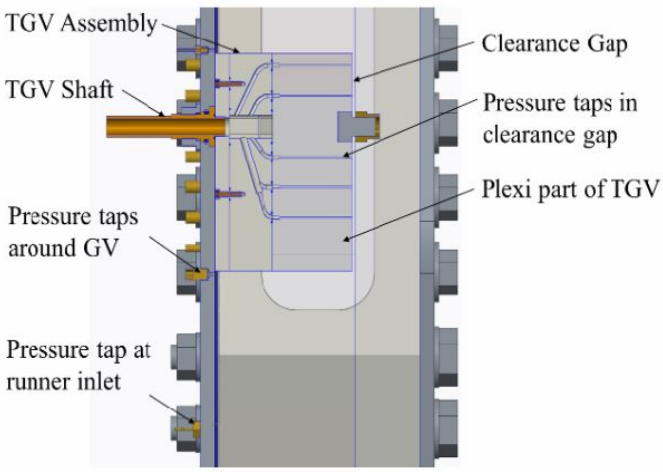


Figure 7.5: Detailed view of test section [**Thapa**, **2016**]

Unlike the previous GV designs used in the test rig, the NACA 4412 guide vane will not have embedded pressure taps in the body of the guide vane. Also since the new GV geometry is asymmetric and not symmetric, the pressure taps on the wall, designed for the initial geometry, will not be perfectly distributed along the GV surface. Some will be partially covered and some will lie a bit away from the surface. This must be remembered when comparing the old pressure measurements with the new ones.

## 7.3 Velocity measurements

To capture the velocity field in the One GV Cascade, Particle Image Velocimetry methods was used. The system was controlled with software from Dantec Studios and used a Nd-YAF laser with a thickness of 1 mm. The illuminated flow field was captured by a HiSense 2M CCD PIV camera at 150 microseconds and 4Hz.

**Optimizing experimental conditions**
It is important to ensure optimized conditions of the experimental setup seen in fig 7.6. Several procedures must carried out each time before starting up the laser and capturing images. These are described thoroughly in the appendix G.1 and will only be described in short detail here.

Checking the alignment and positioning of the camera and laser will ensure that the camera captures the wanted flow area, the laser lights up the wanted plane in the flow section and similar experimental conditions in each experiment.

To be able to capture the flow accurately, the laser energy must be maximized at 10 mJ, the number of particles must be sufficiently large for the software to produce realistic velocity plots and the image capturing time must be adjusted to the particle velocity so that it's within the software's min and max "detection range".

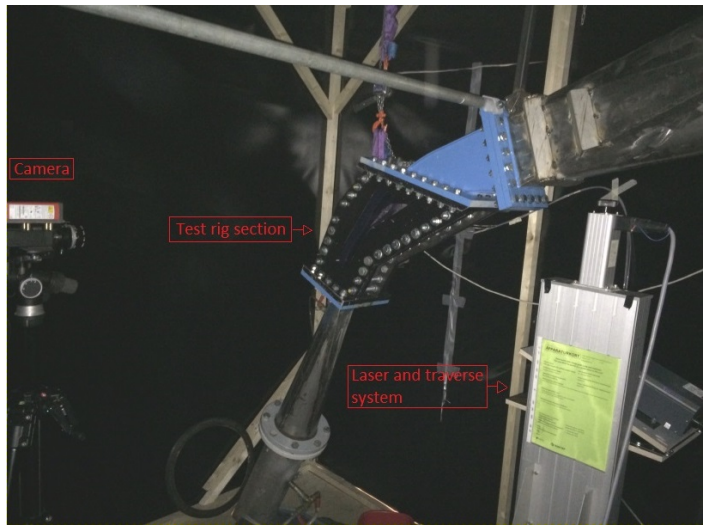


Figure 7.6: Test rig and PIV setup

**PIV image processing**
To process the captured images, software from Dantec Dynamics was used. The software has several tools to process, analyse and improve the quality of the results. These will only be described briefly, a more detailed description of the

processes can be found in appendix G.2 and G.3.

After capturing images of the flow, it is normal to remove the areas of no interest with the Image Masking method. Another important method is the "Image Min/Max", where the common background in every picture was isolated. By applying the "Image Arithmetic" method, this background was subtracted from all the pictures. After this, the final processed pictures will only consist of the illuminated particles.

By using Cross Correlation method, the software tracks the particles movement between every picture and creates velocity vectors. With a further analysis of this vector plot with the Universal Outlier Detector and Moving Average Validation method, bad vectors was removed. By applying Vector Masking, vectors created outside the area of interest was also removed. The final velocity plot is produced with the Vector Statistics method. This produces one final velocity plots based on all the processed vector plots as seen in figure 8.7 in chapter 8.

# Chapter 8

# Results

By doing an experimental and CFD analysis on both the symmetrical and asymmetrical guide vane profile it is possible to study which design is the best to reduce sediment erosion in the turbine system. Experimental studies has already been done on the initial GV design(NACA 0012) in 2015. Through experiments on the NACA 4412 profile, it is possible to validate the CFD results that indicated that NACA 4412 would be a better GV design. These data enables a comparison of both the CFD and the PIV results of the two profiles, both separately and together.

## 8.1 CFD analysis of test rig water flow

As mentioned before, only results from CFD and experimental analysis on NACA 0012 and 4412 will be presented in this thesis. This was decided after an initial CFD analysis done by PhD student Sailesh Chirtackar at the Water Power Laboratory at NTNU. He did a CFD analysis on different GV design in the One GV Cascade test rig. The different foil designs were NACA 1412, 2412 and 4412. The results was compared with the initial reference design(NACA 0012) and it was concluded that the NACA 4412 had the most promising results. To further investigate and validate these results, this thesis will present a further study of the chosen GV geometries.

**Flow around GV**
After running a CFD analysis with the k-epsilon turbulence model, good results was obtained as seen from the figures 8.1a and b. The speed in NACA 0012 quickly accelerates in the suction side from about 5 m/s before the GV to about 12 m/s just before the trailing edge of the GV. At the suction side of NACA 4412 the flows behaviour is quite different. As seen in figure 8.1b, the flow accelerates lot more gradually and reaches its highest value close to the trailing edge with a velocity of about 10 m/s.

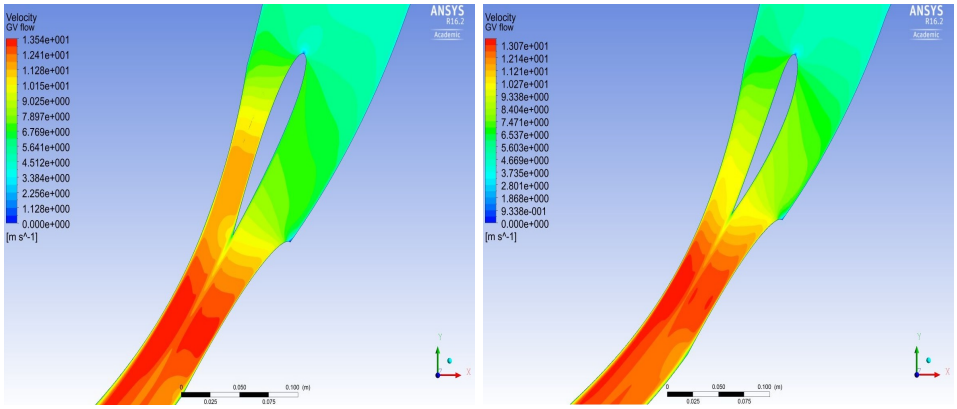


(a) NACA 0012 (b) NACA 4412

Figure 8.1: GV midsection flow

At the pressure side of the guide vanes there is also a difference in the velocity distribution. In the reference design, the velocity does not change a lot before close to the trailing edge(TE), where it reaches 10 m/s. In NACA 4412 the acceleration happens a lot earlier and more gradually than in the reference design. This might come from a more equalized pressure difference between the pressure and suction side of the guide vane. This will become more clear as the pressure results are evaluated.

Both of the velocity plots distinctly show the effects of the GV wake as seen in 8.3b. The wake has shifted position for NACA 4412, probably as a result of its different geometry and pressure distribution. The average deviation between the results is 1.7% and it is clear that NACA 4412 has a lower $C_u$ velocity everywhere except in the GV wake.

**Flow in clearance gap**
As mentioned in the paragraphs above, the guide vane profile NACA 4412 clearly show different velocities around the GV. This will also affect the clearance gap flow, the filament vortex and as a result the erosion in the whole system. The contour plots of the clearance gap flow shown in figures 8.2a and b, shows a considerable higher CG flow in NACA 0012. Especially in the area towards the TE of the GV, where the velocity reaches about 13 m/s.

The trends seen in the velocity plots indicated that a high pressure difference between the two sides of the GV drives the CG flow. Unlike the reference case, the CG velocities in the NACA 4412 case does not reach higher than about 7-8 m/s. This is substantially lower than in the reference design.

In more detail, the velocities along the GV chord line in the CG are plotted in figure 8.3a. The total average deviation is 15.7% with the biggest difference from about 40% to 85% of the chord length, after this the pressure difference

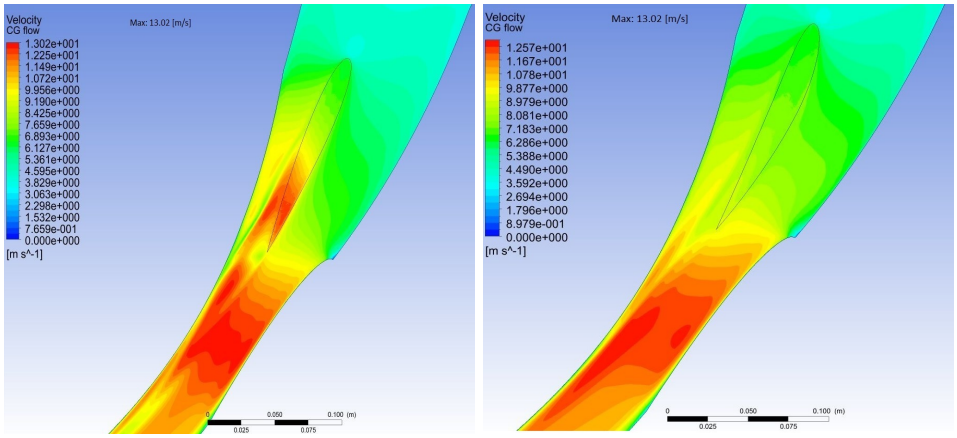


(a) NACA 0012 (b) NACA 4412

Figure 8.2: Clearance gap flow

gradually equalizes towards the trailing edge. This is also visible in 8.2a, where the accelerated water from the clearance gap moves towards the test rig wall and away from the increasing pressure towards the TE.

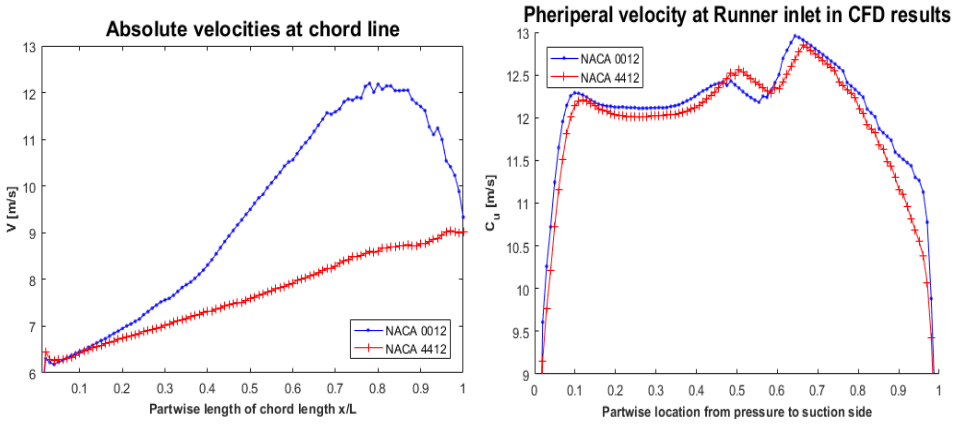


(a) Velocities at chord line in CG (b) $C_u$ velocities at runner inlet

Figure 8.3: Test rig velocities

Another important aspect of the clearance gap flow is its direction. The bigger the angle between the CG flow and the free-stream flow, the more the free-stream flow will be disturbed. By plotting stream lines in the CG plane of the CFD results, it is possible to visualise how the water flows through the CG.

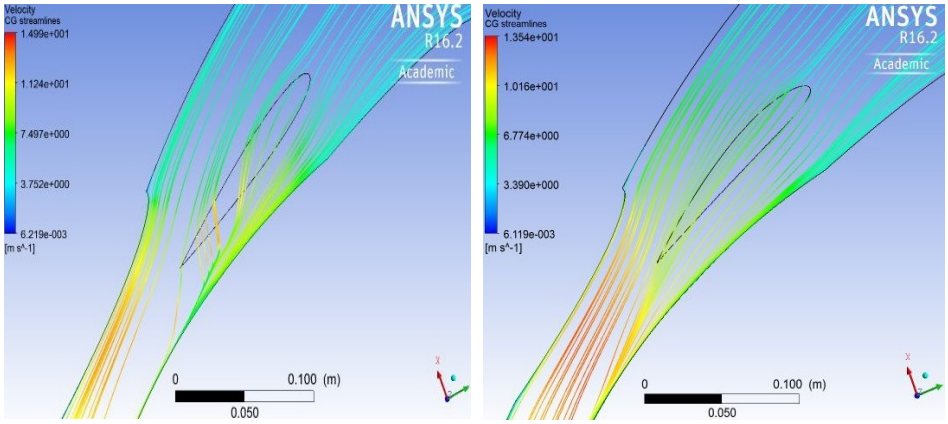


(a) NACA 0012 (b) NACA 4412

Figure 8.4: Streamlines in CG

Figure 8.4a and b shows the difference in the direction of the CG flows. In the initial design, the flow at the pressure side of the GV, will suddenly change direction, go through the CG and over to the suction side. At the suction side, it is also clear that the flow will be pushed towards the test rig wall. In NACA 4412, the flow in CG will be relatively undisturbed. It is possible to see some effects of the small pressure difference, but it is minimal compared to flow in the reference design.

**Pressure distribution on GV**

The flow described and seen in the figures above, is probably caused by two very different pressure distributions around the GV profiles. By plotting a normalized pressure distribution over the GV, both pressure distributions can easily be studied. For the two guide vanes that have been used in this study, these plots can be seen on the next page. In NACA 0012 there is a large difference between the pressure at the suction side and the pressure side. The low pressure on the suction side causes the high velocities seen in the velocity contour plots for NACA 0012.

This difference is the main cause of the high CG flow and as an effect the creation of the filament vortex. Especially towards the TE, the pressure difference for NACA 0012 becomes larger, which explains the mentioned increase in its velocity close to the TE. In the pressure plot for NACA 4412 the pressure difference is a lot smaller. The difference between 8.11a and b becomes very clear from about 30% of the chord length towards the TE. The result of this different pressure distribution causes a lower CG flow seen in figure 8.2b. A smaller CG flow, should also cause a weaker filament vortex.

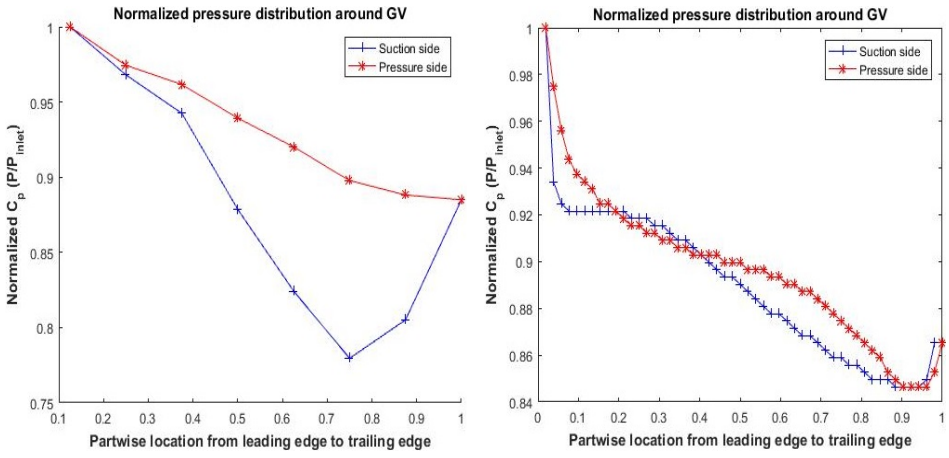


(a) NACA 0012 (b) NACA 4412

Figure 8.5: Pressure results - CFD analysis

**Filament Vortex**

The leakage flow clearly seen in the reference design creates a filament vortex that can be observed in Ansys. This vortex causes severe sediment erosion downstream in the system. If the new GV design manages to reduce this vortex, the sediment erosion in the turbine system would also decrease. In other words, important observations can be made from studying the two vortices seen in figure 8.6.

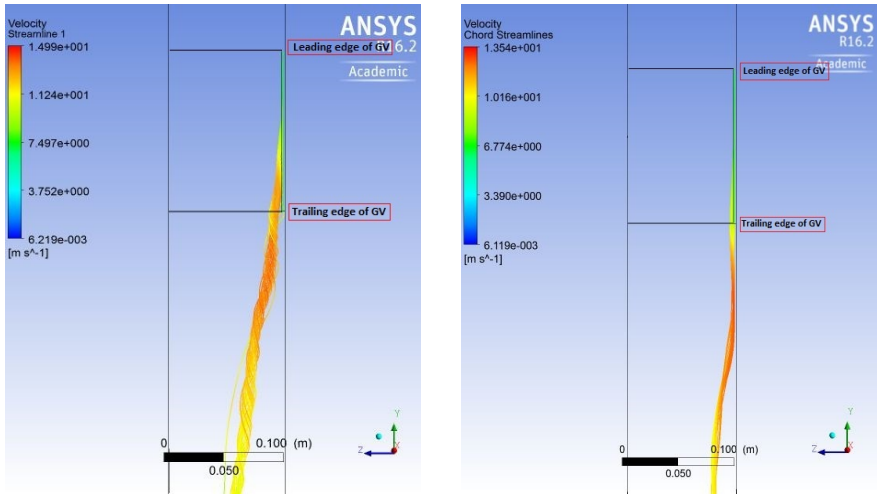


(a) NACA 0012 (b) NACA 4412

Figure 8.6: Filament vortex

In the reference design, the vortex is bigger, has higher velocities and goes further towards the center of the test rig flow compared to the NACA 4412 case. In this case, the vortex does also not appear to have the same size or circulation as the reference design. These are all indications that using a NACA 4412 would reduce the sediment erosion in the system.

## 8.2 Experimental analysis of test rig water flow

To further validate the results that were found in the CFD analysis, the NACA 4412 profile was also investigated in the One GV Cascade test rig at the Water Power Laboratory at NTNU. These experimental data can be compared with both previously done PIV measurement on the reference design and with the CFD results discussed earlier in the thesis.

**PIV analysis of velocity distribution**
As described more in detail earlier, a PIV laser system was used to investigate the water flow in the test rig. With the help of the PIV analysis software, Dynamic Studios, it is possible to create accurate vector plots. The software uses methods for particle tracking as seen in 8.7a. By applying post processing methods on the 200 velocity plots, the software substitutes "bad" vectors and produces one final velocity plot as in 8.7 b.

This makes it possible to produce relatively accurate final result in areas where there often is a lack of good vectors in initial velocity plots. This might happen in areas where there is lack of laser light because of impurities or optical distortions. In the test rig this happened behind the LE and TE of the GV and at a bend downstream of the GV as seen in 8.7 a.

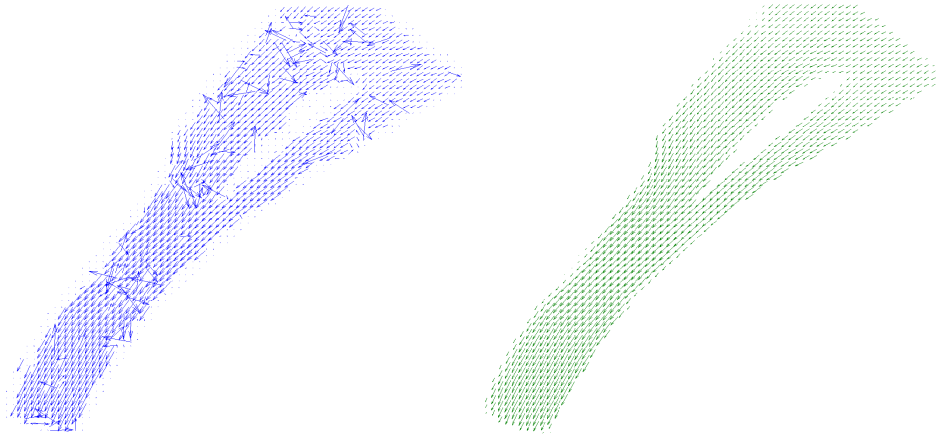

(a) Initial velocity plot (b) Final velocity plot

Figure 8.7: PIV velocity plots - NACA 4412

The jagged boundaries of the contour plots are caused by the masking and the square interrogation areas. It is important to mention that this is not caused by uncertainties in the measurements close to the edges. By exporting these data to Matlab they can be further investigated and compared to other PIV and CFD results.

**Flow around GV**
The PIV results of the flow in the test rig midsection, shows some of the same tendencies as the CFD results. There is a relatively small velocity difference between the two sides of the GV. As in the CFD velocities the flow reaches about 10 m/s at the suction side. The acceleration is also a lot lower than in the results from the CFD and PIV analysis on NACA 0012. Downstream of the GV, the PIV results are not able to show the effects of the GV wake. It is only barely visible close to the trailing edge of the guide vane.

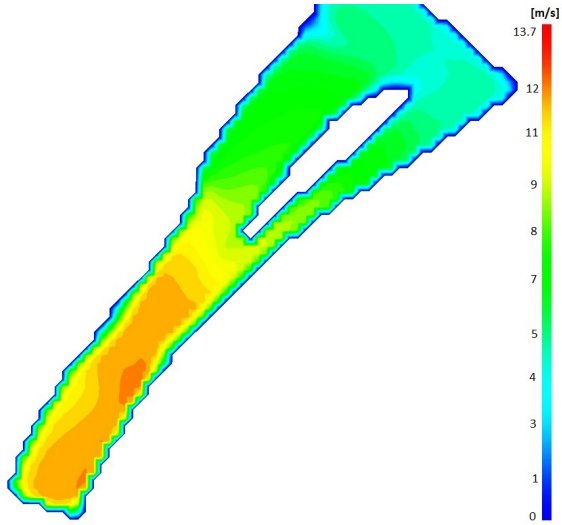


Figure 8.8: PIV contour plot - NACA 4412

With the help of Matlab, it is possible to compare and evaluate the CFD and PIV result in detail. This is done below in 8.9, where the $C_u$ velocities 5 mm above the runner inlet has been studied. Because of a limitation in the PIV images, both the CFD and the PIV velocities had to be evaluated a bit upstream of the runner inlet.

The $C_u$ velocities seen in figure 8.9, follow almost the same trends. One main difference is that the PIV result is not able to capture the effects of the GV wake. This fits well with what the contour plot indicated earlier. The PIV captured $C_u$ velocities are also higher than the CFD results at the suction side of the flow channel. The total average deviation between the CFD and the PIV results is 5.8% at the line evaluated.

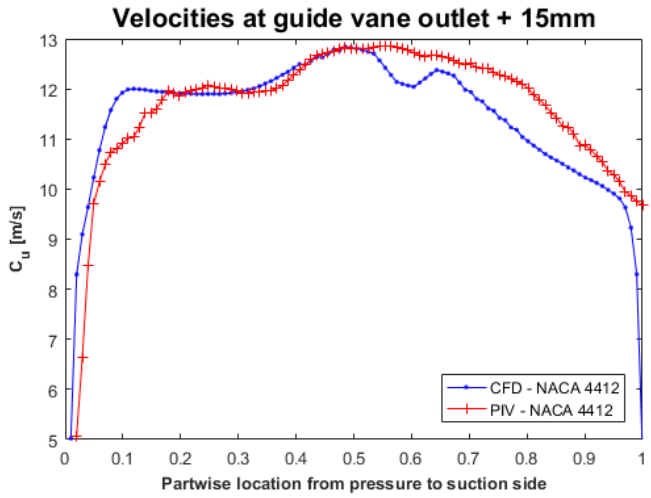


Figure 8.9: $C_u$ velocities at runner inlet

**Flow in clearance gap**

The PIV captured clearance gap flow shows the exact same trends as the CFD results indicates. In 8.10a you can clearly see how the direction of the clearance gap flow is different than for NACA 4412. The flow have the same direction as shown in the CFD results in figure 8.4a. For the case of NACA 4412 the CG does not have the same "drastic" change in direction as in the original GV design.

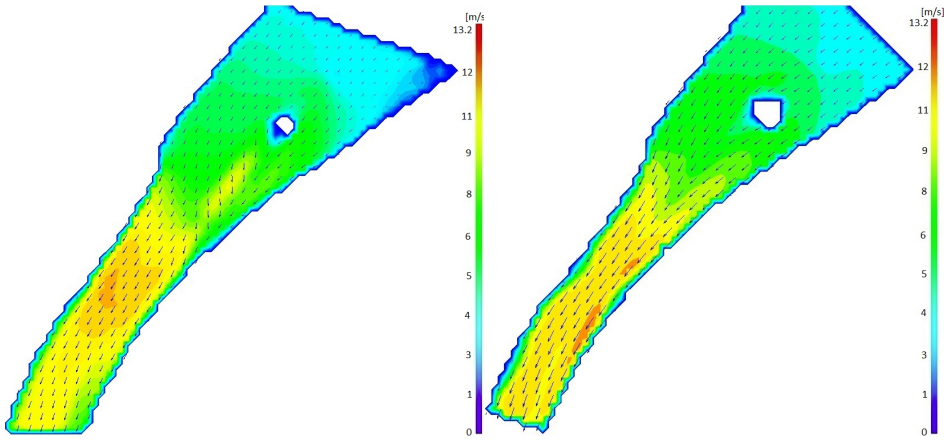

(a) NACA 0012 -Results fall 2015 (b) NACA 4412 - Results spring 2016

Figure 8.10: PIV captured flow in CG

Since the PIV results follow the same trends as the CFD, it can be seen as a good validation of the CFD results.

**Pressure measurements**

Even though the pressure taps in the test rig will not always be completely close to the new GVs surface, it will still give good indications of the pressure distribution around the GV.

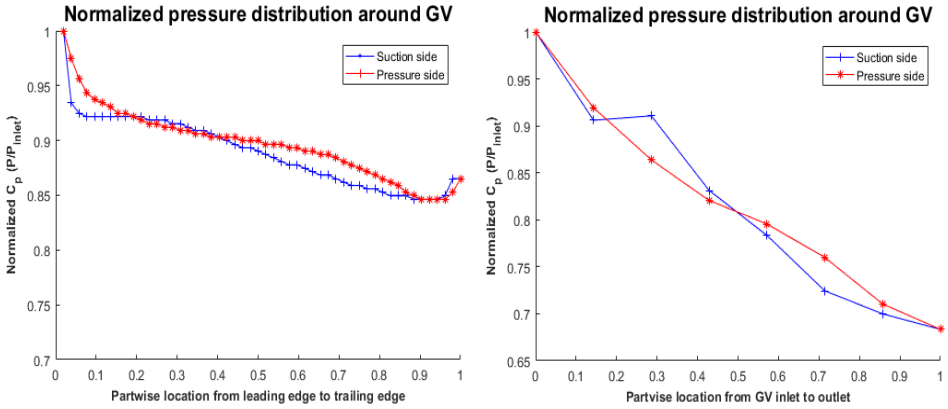


(a) CFD results

(b) Experimental measurements

Figure 8.11: Pressure results NACA 4412

In the experiments, the pressure at the outlet of the test rig had to be maintained at a certain level to avoid cavitation. This causes a pressure deviation at the outlet of the actual test rig compared to the CFD analysis.

The deviation will affect the pressure distribution seen in figure 8.11b, with a lot lower pressure coefficient towards the TE compared to the CFD analysis. Even though the results can not be directly compared, the tendencies can be evaluated. The results follow the same trends, with a significantly improved pressure difference compared to the initial GV design. This can be seen as a further validation of the CFD results.

There is a slight deviation of the main trends towards the trailing edge of the guide vane. While mounting the GV in the test rig, the GV got a small deviation in the angle. This made the trailing edge to lie a bit away from the last pressure tap. This might be one of the reason for the deviation in the two results close to the TE. Ideally there should also have been more pressure taps around the GV body. This could also reduce the deviation between the two results.

## 8.3 Sediment erosion simulation

By inserting particles in to the flow it is possible to use CFD to analyse where the sediment erosion will occur. The particles was defined with the same properties as Quartz and was inserted evenly in to the inlet of the test rig. The Tabakoff and Grant erosion model and Finnie's model was used to simulate the erosion in the system.

After running simulations with both of CFX erosion models, it became clear that the models only accounted for erosion with a relative high impact angle. The models did also not include abrasive erosion.[**Ansys**] This was obvious from the fact that the only erosion patterns was at the LE of the GV, as shown from the results in figure 8.12. Therefore it was concluded that the results could not be used to further validate the improvement in the flow conditions with NACA 4412 as GV design.

Finnie's erosion model showed the same result as "Tabakoff and Grant," with a scattered pattern on the LE of the guide vane. Since non of the results was evaluated in detail, only the Tabakoff and Grant erosion result is presented.

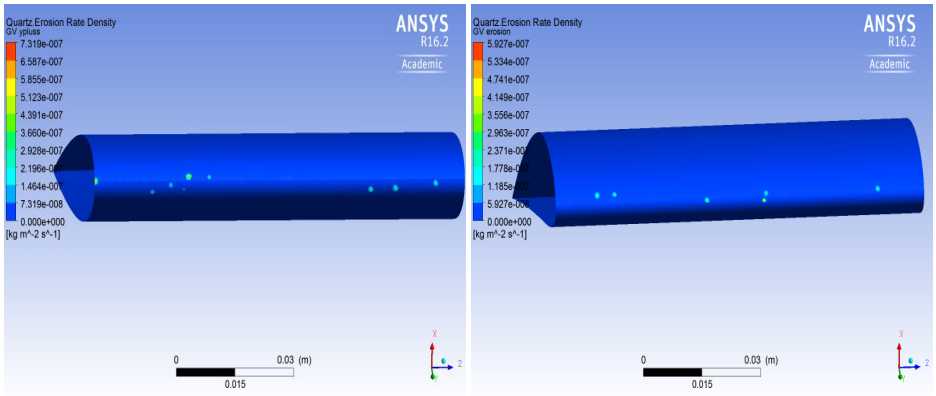


(a) NACA 0012 (b) NACA 4412

Figure 8.12: Tabakoff - Quarts erosion rate density

In Ansys Fluent there are more advanced options to simulation erosion, which also accounts for abrasive erosion. Because of limited knowledge about Ansys Fluent and the limitation of time, further simulations with sediment erosion was not done. This has also been mentioned in the future work section.

## 8.4 Validity of comparison

To ensure that the two different GV profiles are compared on the same grounds, properties of the flow must be checked. One important property is the inlet pressure of the test rig. This must be similar for the comparison to be 100% valid. If not, this will also change the design H of the system.

This was done in CFD post, by comparing the average pressure at the inlet of the test rig. NACA 0012 had $P_{ave}$=325236 Pa. In the NACA 4412 simulation, the pressure at the inlet was $P_{ave}$=320638 Pa. This is a deviation of 1.4%. This is not a large deviation, but the deviation would probably propagate in a complete turbine system. This might also be the cause of the deviation of 1.7% in the $C_u$ velocities at the runner inlet of the two guide vane designs. In other words, by only changing the reference GV with the new design, the pressure in a complete turbine system would probably propagate even more than in the One GV Cascade case.

Additional simulations was done to see if changing the angle of the NACA 4412 guide vane could reduce the pressure difference to the initial results of the reference design. The results are presented in table 8.1, and clearly shows a pressure difference even after changing the GV angle. In other words, further analysis on a new test rig should be done. A new test rig designed from a complete turbine system with NACA 4412 as GV geometry. This could further validate the results through new tests in an improved test section.

Table 8.1: NACA 4412 angle test

| GV angle [deg] | Pressure new GV design [Pa] | Deviation from reference design [%] |
|---|---|---|
| 0 | 320638 | 1.41 |
| 0.5 | 321620 | 1.11 |
| 1 | 320882 | 1.34 |
| 2 | 320907 | 1.33 |
| -0.5 | 318243 | 2.15 |
| -1 | 317859 | 2.27 |
| -2 | 319536 | 1.75 |

## 8.5 Uncertainty in experiments

**Uncertainty in velocity measurements**
The uncertainty analysis of the PIV results has been one of the biggest challenges in this master thesis. A lot of time was used trying to follow ITTC'- recommended procedures and guidelines for uncertainty analysis of PIV experiments. [**ITTC 2008**]

This guideline describes the systematic error in the camera, laser, software and the general experimental setup. Because of insufficient knowledge on how to make realistic assumptions for the out of plane movement and mis-matching error, a realistic systematic uncertainty was not found.

A student-t distribution was applied to the calculated velocity plots, the random uncertainty at each calculation point can be evaluated. By calculating the average and standard deviation in the velocity of each interrogation area, the average random uncertainty is calculated to be 1.4%. The uncertainty in each of the interrogation areas can be seen in figure 8.13.

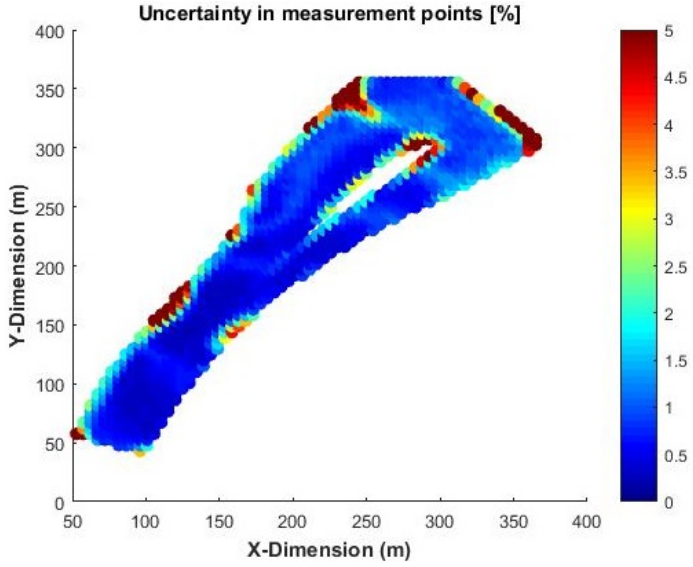


Figure 8.13: Uncertainty in PIV velocity plot

The areas with the highest uncertainty correlates well with the areas which receives less laser lighting. This is the areas behind the LE, TE and at the bend of the test rig. Further work has to be done to study the systematic error from the camera, laser and the software. When this is found, the total uncertainty of the measurements can be calculated through the formula $\sigma = \sqrt{\sigma_S^2 + \sigma_R^2}$

**Uncertainty in pressure measurements**

The uncertainty in the pressure readings was calculated based on the uncertainties of the calibration results and the pressure measurement. The uncertainties are presented in the table below, and the basic theory of behind the uncertainty analysis is given in appendix D.

Table 8.2: Uncertainty in pressure measurements

| P. sensor | Uncertainty [%] | Uncertainty [Pa] | P. sensor | Uncertainty [%] | Uncertainty [Pa] |
|---|---|---|---|---|---|
| 1 | 0.24 | 0.32 | 8 | 0.11 | 0.10 |
| 2 | 0.17 | 0.21 | 9 | 0.32 | 0.30 |
| 3 | 0.13 | 0.15 | 10 | 0.46 | 0.45 |
| 4 | 0.12 | 0.13 | 11 | 0.28 | 0.29 |
| 5 | 0.11 | 0.12 | 12 | 0.64 | 0.71 |
| 6 | 0.20 | 0.20 | 13 | 0.15 | 0.19 |
| 7 | 0.11 | 0.10 | 14 | 0.20 | 0.24 |

# Chapter 9

# Discussion

**Unstructured mesh**
In the meshing of the One GV Cascade, Ansys meshing has been used with sizing methods to control the maximum element size in specific areas of the test rig. After comparison with previous meshing methods on the One GV Cascade, it became obvious that this method was costly in computational time and gave smaller control in scaling of the mesh.

By meshing in e.g. ICEM, a user could more easily have increased the density of the mesh in even more specific areas of interest as the GV wake area. Other methods would also have given a lot easier scaling of the mesh during the mesh independency test. The body sizing method forces the user to slowly increase the density of the mesh, and checking if it was close to a wanted density e.g. 2, 4 or 6 million cells. Even though the computational cost will be greater, the results will be valid based on the results from the mesh independency test.

**Validity of NACA 0012 and NACA 4412 comparison**
The two CFD results show a clear difference of 1.4% in the pressure at the inlet of the test rig. Even when the angle of the new guide vane design was changed, there was still a significant pressure difference. Using the new GV design in a complete turbine system will probably increase the pressure difference even more compared to the reference turbine. This means that the promising results will have to be further validated through more research.

**Choice of turbulence model**
In the CFD simulation the k-epsilon turbulence model was chosen. This was initially done because of the high computational cost of setting up a good mesh for a k-omega SST simulation. After obtaining a better computer, simulations for a $k-\omega$ SST turbulence model was run. The mesh was optimized for this turbulence model, with $y^+_{ave} = 1$ The results were the same as the initial ones obtained with $k-\epsilon$. It was therefore concluded that the results from the $k-\epsilon$ could bee seen as valid.

**Deviation between PIV and CDF results**
The trends seen in figure 8.9 shows that the $C_u$ velocities at guide vane outlet + 15 mm are quite similar for the CFD and the PIV results. The average deviation is at 5.9% and is similar to deviation obtained in earlier PIV measurements. One of the main differences is that the PIV measurements are not able to capture the GV wake close to the runner inlet. One of the main reasons for this is probably the moving average validation method used to produce the final vector plot. This will smooth out the "sharp" velocity difference between the GV wake vectors and the ones close to it.

# Chapter 10

# Conclusions

There is a obvious difference in the flow around the two different guide vane designs. In the reference design, the CFD results show a clear velocity difference between the suction side and the pressure side. The suction side reaches about 12 m/s and experiences a higher acceleration compared to the pressure side. In the pressure side, the highest velocity is close to the trailing edge at about 10 m/s.

With the new GV design, there is a much lower velocity difference between the two sides of the GV. The highest velocity, of 10 m/s, occurs at the suction side, close to the TE. The acceleration is a lot more gradual both at the suction side and at the pressure side. All this indicates a much lower and ideal pressure difference over the new guide vane design.

Downstream of the GV, both CFD results shows high velocities and clear effects of the GV wake. At the runner inlet, the $C_u$ velocities follows the same trends and only deviates with 1.4%. The $C_u$ in NACA 4412 is consistently smaller everywhere except in the GV wake where the NACA 4412 shows higher values. The main deviation is probably caused by the new GV geometries change of the pressure at the inlet.

The CFD results also shows a clear improvement of the CG flow with NACA 4412 as GV profile. With a lot lower absolute velocity the filament vortex both becomes smaller and weaker. All of these indications are further validated by the experimental results. In the PIV contour plot, the measured velocities follow the same trends as the CFD flow. Both with an improved clearance gap flow, improved velocities around the GV and a smaller measured pressure difference.

Even though everything indicates that NACA 4412 is a much better GV design to reduce erosion, further research has to be done to verify this. By designing a new test rig based on a turbine system with NACA 4412 as guide vanes, more accurate and valid experiments can be done. This would hopefully further validate the results and be the next step in the development of an improved guide vane design.

# Chapter 11

# Further work

**Redesign test rig**
Since the test rig walls are designed by "neighbouring" NACA 0012 GVs, this will probably affect this result. To replicate more realistic flow conditions for the NACA 4412 GV, a new test rig should be designed. The walls of the new test rig should be designed by neighbouring NACA 4412 as thoroughly described for the initial test rig earlier in the thesis.

**Improve uncertainty analysis**
A further study of the uncertainty analysis in the PIV results has to be done. Through ITTC guidelines for systematic uncertainty analysis in PIV measurements a total systematic uncertainty of about 10% has been obtained. Because of some uncertainty in whether the method is directly applicable to this thesis experiments, improvements must be done. A new method must be found, or better assumptions for the uncertainty in the "out of plane movement" and "mis-matching error". By improving the uncertainty analysis the results can be trusted and verified in a better way.

**Erosion simulations**
After running both Tabakoff and Finnie's erosion models in Ansys CFX, it was clear that the models only accounted for erosion with a relative high impact angle. Neither model accounted for abrasive erosion. By using Ansys Fluent instead of CFX, the flow in the test rig can be simulated with better erosion models which includes abrasive erosion. This would allow a much more detailed analysis of how the fluid flow will affect the erosion in the system. Then the erosion pattern in the CG and along GV surface will hopefully be a lot more clear.

# Bibliography


[1] S. B. Pope. *Turbulent Flows*, 6th ed. Cambridge University Press.

[2] Y. A. Cengel and J. M. Cimbala. *Fluid Mechanics: Fundamentals and Applications*, 6th ed. McGraw-Hill, 2012.

[3] G.W. Stachowiak and A.W. Batchelor. *Engineering Tribology. Tribology series,* 6th ed. Elsevier Science, 1993.

[4] B. Thapa. *Sand Erosion in Hydraulic Machinery, Phd, Trondheim.* Water Power Labaratory, NTNU, 2004.

[5] K. Gjosaeter. *Hydraulic Design of Francis Turbine Exposed to Sediment Erosion, Master thesis, Trondheim*, Water Power Labaratory, NTNU, 2011.

[6] G.A. Dahl. *Hydraulic Design of Francis Turbine that will be influenced by sediment erosion*, Water Power Labaratory, NTNU, 2014.

[7] B.S Thapa. *Hydraulic design of Francis turbine to minimize sediment erosion, Master thesis,*, Kathmandu University, 2012.

[8] F.R. Menter. *Review of the Shear-Stress Transport turbulence model experience from an industrial perspective, Master thesis,*, International Journal of Computational Fluid Dynamics, 2009.

[9] F.R. Menter. *Turbulence modeling, URL*, http://personalpages.manchester.ac.uk/staff/david.d.apsley/lectures/comphydr/index.htm

[10] B.S Thapa, C. Trievedi, O.G. Dahlhaug. *Design and development of guide vane cascade for a low speed number Francis turbine*, Journal of Hydrodynamics, 2015.

[11] B.S Thapa, O.G. Dahlhaug and Bhola Thapa. *Flow field measurement in guide vane cascade of high head Francis turbine*, 6'th Conference On Water Resources and Hydropower Development in Asia, 2016.

[12] P.J. Gogstad. *Hydraulic design of Francis turbine exposed to sediment erosion*, Master thesis NTNU, 2012.

[13] IEC hydraulic machines. *The Comprehensive Treatment of the Sand Erosion on Hydraulic Turbine*, International Electrotechnical Commission, 2008.

[14] I. Iliev. *Analysis of flow in 1 GV cascade (Draft).* NTNU, 2016.

[15] H.K. Versteeg and W. Malalasekera. *Computational fluid dynamics*, Pearson, 2007.

[16] C.G. Duan and V.Y. Karelin. *Abrasive Erosion & Corrosion of Hydraulic Machinery*, Imperial College Press, 2002

[17] M. Raffel, C. Willert and J. Kompenhans. *Particle image velocimetry, A Practical Guide.*, Springer, 1998

[18] H.P. Neopane. *Sediment Erosion in Hydro Turbines*, Phd, NTNU 2010.

[19] International Towing Tank Conference. *Uncertainty Analysis Particle Image Velocimetry.* ITTC, 2008

[20] R. J. Adrian & J. Westerweel. *Particle Image Velocimetry*, Cambridge University Press, 2012.

[21] F. Scarano. *Experimental Aerodynamics.* Delft University of Technology, 2013.

[22] Ansys support. *url:* www.support.ansys.com/staticassets/ANSYS/Conference/Confidence/Hou
modeling-and-sand-management-with-ansys-cfd.pdf

[23] Dynavec. *url:* http://www.dynavec.no/en/francis/technology

# Appendices

# Appendix A

# NACA profiles

NACA profiles are often used as guide vanes in hydro power plants. The NACA profiles are defined by a series of numbers which defines properties of the airfoil. Only 4 digit airfoils will be considered in this thesis.

The first of the four digits is given as the percentage the maximum camber line is of the chord. The second digit represents the distance, in tenths of the chord, from leading edge to the maximum camber. The two last numbers is the percentage the maximum section thickness represents of the chord. All of these dimensions can be seen in figure A.1

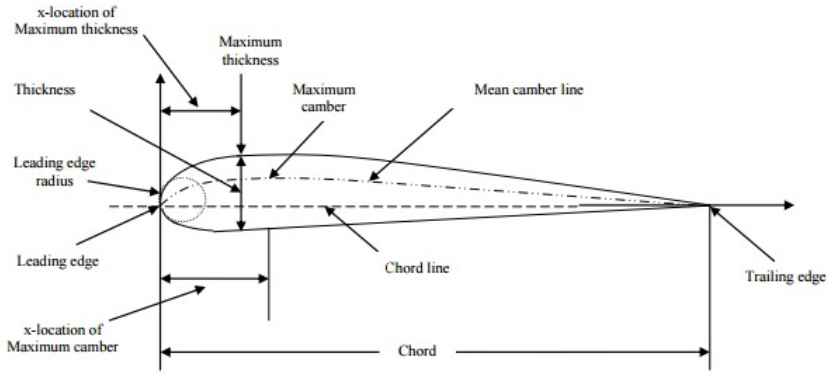


Figure A.1: Airfoil dimensions []

The profiles that will be studied in this paper is the NACA 0012 and 4412. The similarity between these airfoils is the same maximum thickness. The NACA 0012 is a symmetrical airfoil, with the NACA 4112 as asymmetrical airfoils. To study the effects of these different airfoil designs in both CFD and experimental studies will give indications of what design is the best.

# Appendix B

# Mesh quality

Table B.1: Mesh statistics

| Parameter | Value |
|---|---|
| Nodes (Mil) | 5.96 |
| Total Elements (Mil) | 27.3 |
| Skewness | 0.2 |
| Orthogonal Quality | 0.88 |
| Aspect ratio | 3.8 |
| Turbulence | k-epsilon |
| Fluid type | Water at 25˚C |
| Simulation type | Steady state |
| Inlet Condition | Water velocity[m/s]: 0.46 |
| Outlet Condition | Average static pressure (atm): 303 [kPa] |
| Convergence criteria | RMS<1e-04 |
| Advection scheme | High Resolution |

# Appendix C

# Experimental information

| Target Flow of Measurement | | | |
|---|---|---|---|
| Target flow | | | 2-D waterflow |
| Measurement facility | | | 1 GV Cascade |
| Measurement height | | [mm] | 360.3 |
| Measurement width | | [mm] | 480.3 |
| Uniform flow speed | | [m/s] | 5 |
| Calibration | | | |
| Distance of reference points | $l_t$ | [mm] | 251.03 |
| Distance of reference image | $L_t$ | [pixel] | 1018.428 |
| Magnification factor | α | [mm/pixel] | 0.246487724 |
| Flow Visualization | | | |
| Tracer particle | | | Spherical nylon particle |
| Average diameter | $d_p$ | [mm] | 0.05 |
| Standard deviation of diameter | $s_p$ | [mm] | 0.005 |
| Average specific gravetyr | | | - |
| Light source | | | Double pulse ND:YAG laser |
| Laser power | | [mJ] | 10 |
| Thichness of laser light sheet | | [mm] | 3 |
| Time interval | | [s] | 1.50E-04 |
| Image detection | | | |
| Spatial resolution | | | 1600 x 1200 pixels |
| Samling frequency | | [Hz] | 8.8 |
| Grey scale resolution | | [bits] | 10 |
| Cell size | | | - |
| Optical system | | | - |
| Distance from the target | | [mm] | 1177 |
| Length of focus | | | - |
| Perspective angle | | [rad] | 0.1347 |
| Data processing | | | |
| Correlation area size X | | [X x X pixels] | 32 |
| Search area size X | | [X x X pixels] | 16 |
| Sub-pixel analysis | | | 5 points Gaussian fitting |

Figure C.1: Change this to spring values

# Appendix D

# Uncertainty

The uncertainties for a measuring point consists of the uncertainty of the calibration and the random uncertainty in each measurement point.

The random uncertainty can be found by computing the standard deviation and the mean value of all the samples. The standard deviation can be calculated as follows:

$$S_Y = \sqrt{\frac{\sum_{i=1}^{n}(Y_i - \bar{Y})^2}{n-1}} \tag{D.1}$$

$Y_i$ is the sample value, the $\bar{Y}$ is the mean value of the samples and n is the number of samples. The student-t distribution with a 95% confidence interval can be expressed as:

$$\bar{Y} \pm t \cdot S_Y \tag{D.2}$$

The student t is a variable dependent on the number of measurements, and can in this case be assumed to be 1.96. The lower and upper bounds of the measured point can now be expressed as:

$$\bar{Y} - \frac{t \cdot S_Y}{\sqrt{n}} \quad < \quad Y \quad < \quad \bar{Y} + \frac{t \cdot S_Y}{\sqrt{n}} \tag{D.3}$$

The random uncertainty in a measuring point can then be expressed through the equation for $f_X$

$$e_x = \frac{t \cdot S_Y}{\sqrt{n}} \quad -- > \quad f_x = \frac{e_X}{\bar{Y}} \tag{D.4}$$

The uncertainties of the calibration can be defined as random and a systematic uncertainty expressed as $f_{Rcal}$ and $f_{Scal}$. By combining the uncertainty of the

calibration and the random measuring uncertainty, we can express the total uncertainty in a measurement as:

$$f_{test} = \sqrt{(f_{Scal})^2 + (f_{Rcal})^2 + (f_x)^2} \tag{D.5}$$

# Appendix E

# Pressure calibration

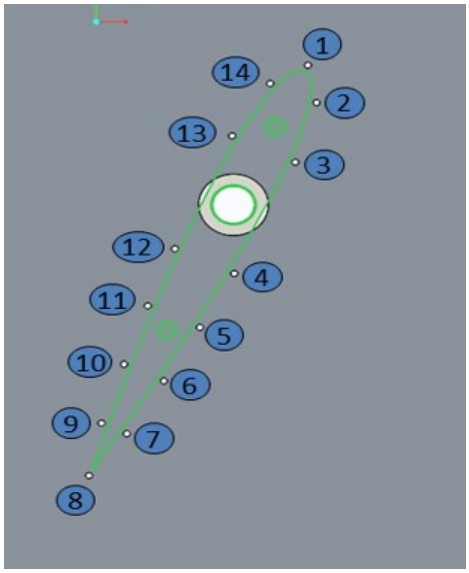


| Pr. Point | Max bar | Ch No |
|---|---|---|
| 1 | 10.0 | 13 |
| 2 | 10.0 | 14 |
| 3 | 7.0 | 11 |
| 4 | 7.0 | 12 |
| 5 | 7.0 | 9 |
| 6 | 7.0 | 10 |
| 7 | 3.5 | 7 |
| 8 | 7.0 | 8 |
| 9 | 7.0 | 5 |
| 10 | 7.0 | 6 |
| 11 | 7.0 | 3 |
| 12 | 2.0 | 4 |
| 13 | 2.0 | 1 |
| 14 | 3.5 | 2 |

Figure E.1: Pressure sensor placement and sensor information

Digital Pressure sensor calibration results

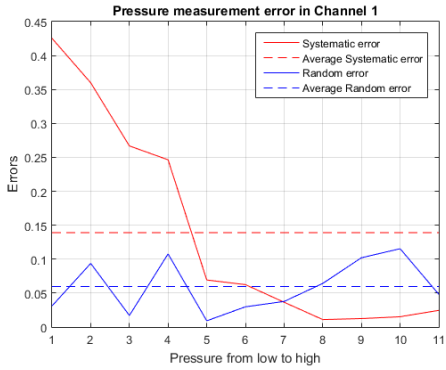


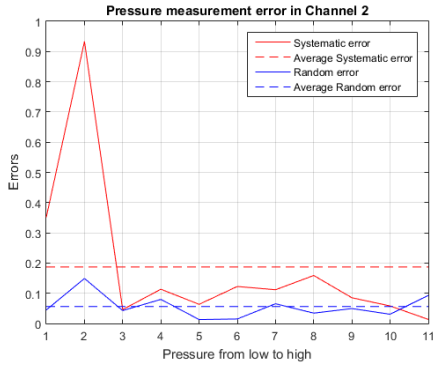


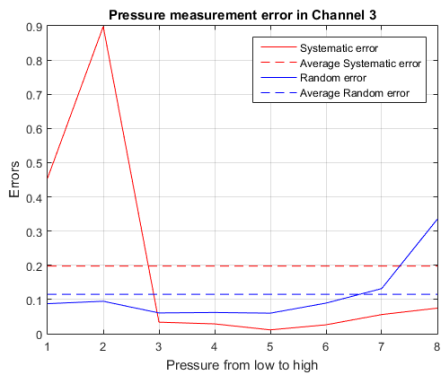


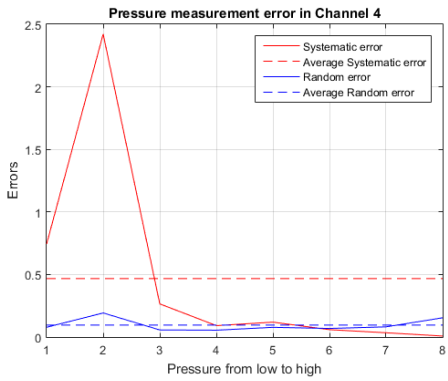


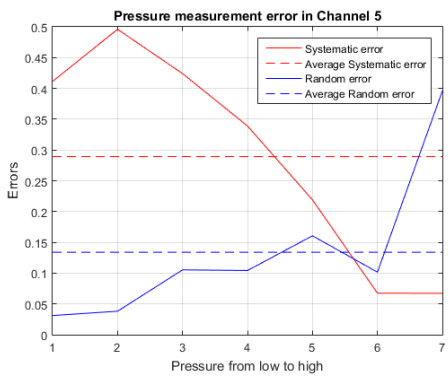


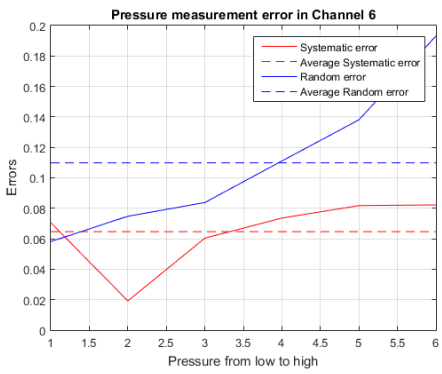

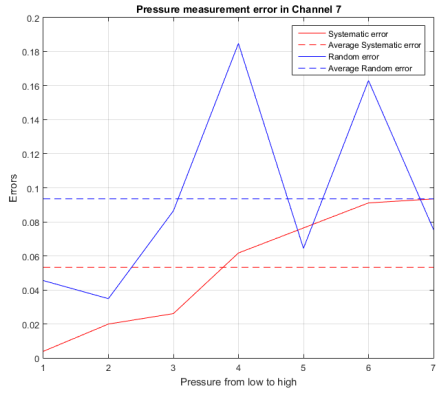
Pressure measurement error in Channel 7
Systematic error
Average Systematic error
Random error
Average Random error
Errors
Pressure from low to high

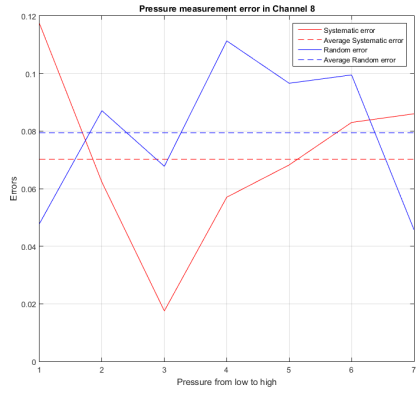
Pressure measurement error in Channel 8
Systematic error
Average Systematic error
Random error
Average Random error
Errors
Pressure from low to high

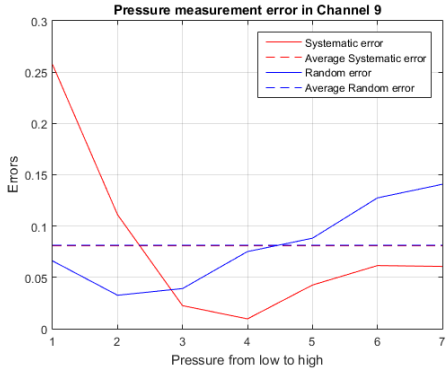
Pressure measurement error in Channel 9
Systematic error
Average Systematic error
Random error
Average Random error
Errors
Pressure from low to high

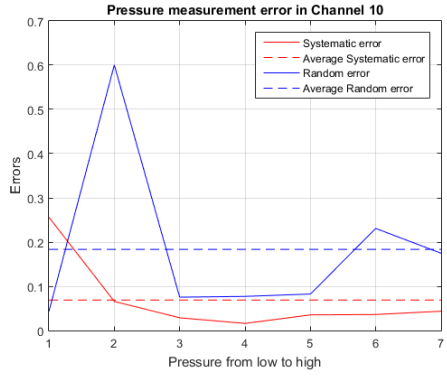
Pressure measurement error in Channel 10
Systematic error
Average Systematic error
Random error
Average Random error
Errors
Pressure from low to high

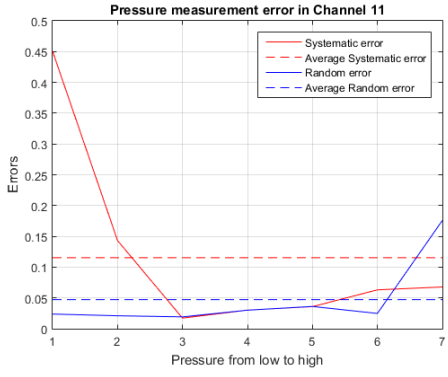
Pressure measurement error in Channel 11
Systematic error
Average Systematic error
Random error
Average Random error
Errors
Pressure from low to high

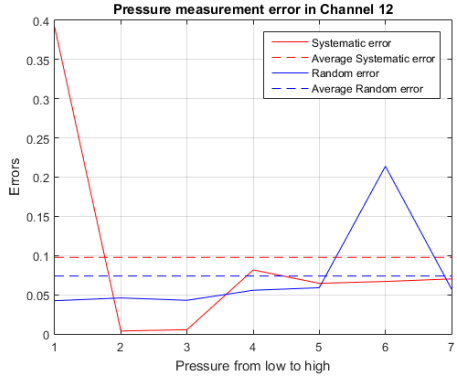
Pressure measurement error in Channel 12
Systematic error
Average Systematic error
Random error
Average Random error
Errors
Pressure from low to high

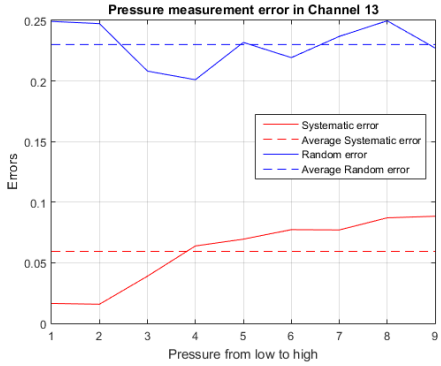
Pressure measurement error in Channel 13
Errors
Pressure from low to high
Systematic error
Average Systematic error
Random error
Average Random error
0
0.05
0.1
0.15
0.2
0.25
1
2
3
4
5
6
7
8
9

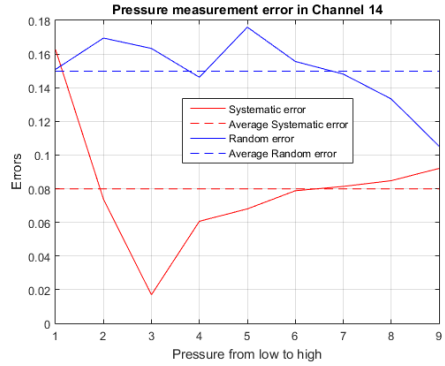
Pressure measurement error in Channel 14
Errors
Pressure from low to high
Systematic error
Average Systematic error
Random error
Average Random error
0
0.02
0.04
0.06
0.08
0.1
0.12
0.14
0.16
0.18
1
2
3
4
5
6
7
8
9

# Appendix F

# Particle Image Velocimetry

**Illumination and light source**
Lasers that emit monochromatic light are widely used in PIV. This is because its ability to emit light with high energy density, through thin sheets of light to illuminate particles. Today's PIV systems usually uses double pulsed lasers. The lasers have to be able to produce light pulses between 5 and 500 mJ to be able to illuminate the particle and form visible images. The specific energy that is needed in a PIV experiments depends on the particles scattering properties. All types of lasers consists of three main components that separates them. These are the laser material, the pump source and the mirror arrangement as shown in figure F.1.

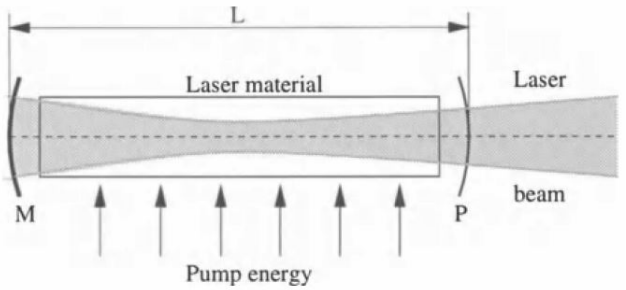


Figure F.1: Laser system schematics.[**Raffel**, **Willert and Kompenhans**, **1998**]

The illuminated sheet in the flow will create a coordinate system in the flow. As shown in Figure 3.1, the coordinates (x,y) the needed variables in the illuminated sheet. The z variable will be the distance from the camera lens. The (X,Y) coordinates defines the coordinate system in the image frame. Because of the lens inverting the image, the coordinates in the image plane (X,Y) will be inverted in respect to (x,y). In other words, a positive displacement in one of the planes with give positive displacement in the other.

## F.1 Calibration and image digitization

**Calibration**
Calibration is a procedure done to identify the image mapping parameter vectors. Determining the image mapping parameters is done to create a relationship between the x=(x,y,z) position in the illuminated sheet and the X=(X,Y) in the image plane.

Determining these parameters is done by inserting a calibration target in the target domain. The target should consist of crosses or dots, to create a grid of markers. By taking several images at different lengths z the image mapping parameter F(x) can be calculated by the software through equation F.1. The $a_i$ parameters represent image mapping parameters.

$$F(x) = a_0 + a_1x + a_2y + a_3z + a_4x^2 + a_5xy + a_6y^2 + a_7xz + a_8yz + a_9z^2 + a_{10}x^3 + a_{11}x^2y + a_{12}xy^2 + a_{13}y^3 + a_{14}x^2z + a_{15}xyz + a_{16}y^2z + a_{17}xz^2 + a_{18}yz^2 \tag{F.1}$$

The target should have a black background with white markers or opposite. To illuminate these markers it is sufficient to use white light source. A laser would not be possible to use because of occurrence of reflections from the reflecting surface. These reflections could destroy the contrast of the calibration image.

**Image Digitization**
The formation of the image is done in the image plane. After this is done, the image is recorded by exposing a photographic film or a video chip like complementary metal oxide semiconductor(CMOS) or a charge-coupled device(CCD). These consists of rectangular or square arrays of sensors that converts the light energy entering in to each pixel in to electrical signals. The signal can be described by function F.2.

$$I[i,j] = \int_{A_{i,j}} \int_{\delta t} p(\mathbf{X}\text{-}\mathbf{X}_{i,j}) I(\mathbf{X},t) d\mathbf{X} dt \tag{F.2}$$

$$= \int_{A_{i,j}} \int_{\delta t} p(\mathbf{X}\text{-}\mathbf{X}_{i,j}) \varepsilon(\mathbf{X}) d\mathbf{X} \tag{F.3}$$

This process of digitizing analogue reading is called pixelization and has got an accuracy of 8 to 12 bits. The signals are first stored in the fast memory and afterwards in the RAM of the computer. To coordinate these events the PIV system uses a synchronizer. The synchronizer controls the arming and firing of the light source, monitoring flow events, opening the camera shutter, activate image acquisition, starting the digitization and transfer of data.

The duration of the time pulse is a lot shorter than the shutter time. To handle the short time, a specially developed camera uses a method called *Single-frame double-pulsed recording* is used. This method records two images on one frame. Another method possible is the *two-frame, single-pulse recording* which is the preferred method. This method uses CCD cameras which is sends the charge fast enough to pixelize both images.

Another problem with the pixelization process is that the accuracy is defined by the pixel size. If the pixel size is bigger than the particle diameter, the particle can at most be placed with a $d_r/2$ accuracy. To reduce this effect, called *pixel locking*, the particles size should be at least 3-5 pixels per particle image diameter.

## F.2 Processing and interrogation

**Image processing**
Different methods in computer software are designed to filtrate out "background noise" and increase the quality of the images. This will make it easier for the software to analyse the flow and give accurate velocity results. These methods used will be discussed further in detail in the experimental description.

**Displacement interrogation**
The image analysis step, is the measurement of the two dimensional image displacement $\Delta \mathbf{X}_P$. Three different basic measurement schemes are used to implement the general measurement scheme. These are 1) low-image density PIV, 2) high-image density PIV and 3) LSV. What differentiates these methods are the concentration of particles. Low-image and high-image density uses low-source-density seeding($N_I << 1$) and LSV uses $N_I >> 1$. This leads both to different methods of interrogation and characteristics.


(a) Low image density

(b) High image density

Figure F.2: Rules for image density

In Scarano, 2013 the operations to evaluate the particle motion was summarized in to 4 points:

1. Image windowing

Dividing the small cells in to smaller interrogation areas, with at least 10 particles. Each "window" becomes a individual measurement, where local velocity vectors are evaluated. These cells are typically in the range of 16x16 to 128x128 pixels.

2. Cross correlation analysis
   Using statistical tracking to the "captured" windows to locate all possible matches. The peaks in the cross correlation map indicates the average particle image displacement.

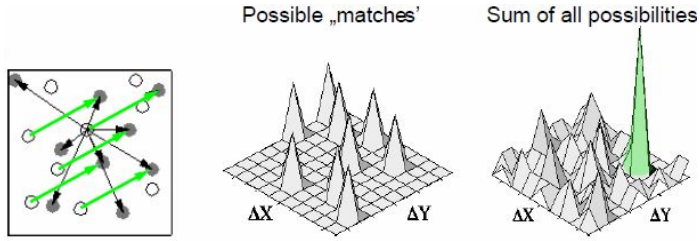


Figure F.3: Cross Correlation method [**Kiger**]

3. Correlated peak sub pixel interpolation
   Through the summation of all the possibilities as shown in figure F.3, it is possible to evaluate which displacement that dominates with the highest peak. This displacement corresponds to the actual motion of the particle.

4. Divide by time and scaling
   To obtain the velocity vector, one needs to change the motion from the term of pixels per second to meters per second. This is calculated by dividing by $\Delta t$, multiplying with the size of the pixel and dividing with the imaging magnification.

**Validating the interrogation**
When analysing the flow with a PIV system there will created a certain percentage of invalid vectors. These invalid vectors can be divided in to two types as seen in F.4. The first type occurs randomly, with no dependence of the velocities in neighbouring cells. The second type of invalid vectors occurs in groups/clusters caused by image distortion on a boundary.
These invalid vectors are in other words caused by large noise peaks or low actual displacement peaks. It is possible to remove these vectors by comparing them to the total average vector or cells close by. The large erratic errors makes the invalid vectors easy to spot and remove.

There are several steps to validate the interrogation. The chosen methods for the analysis is described further in PIV procedures.

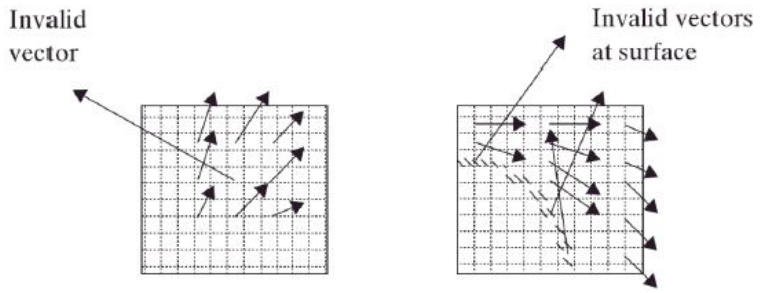


Figure F.4: a) Type 1 is caused by particle grouping within a isolated interrogation area; b) type 2 is caused by image distortion on a boundary. [**Adrian & Westerweel**, **2011**]

## F.3 Rules for optimization of PIV setup

**Number of particles**
$N_i > 10$
The more particles, the better the signal-to-noise ratio will be. The number of particles should be more than 10 per interrogation spot. One can either increase the amount of particles in the flow, or increase the interrogation area to get enough particles.

**Maximum and minimum displacement**
$|\Delta \mathbf{X}| < 0.25 D_i$
The maximum in plane movement should be less than 0.25 of the interrogation are size. This is to ensure minimal out of interrogation area movement and maximization of particle pairing.

$|\Delta \mathbf{X}| > 2 d_p$ The minimum in plane movement should equal two particle diameters.

**Out of plane displacement**
$|\Delta z| < 0.25 \Delta z_0$
The displacement in the out of plane direction should at most be 0.25 of light sheet thickness.

**Image magnification factor**
$\alpha |\Delta u| \Delta t < d_t$
The particle image diameter needs to be bigger than the product of the magnification factor, the absolute variation of the velocity vector and the time.

# Appendix G

# PIV procedures

## G.1 Pre image-capturing procedures

Before starting to capture images, there are several things that has to be checked. The most important is identifying safety hazards and taking the necessary safety measures. To ensure the best results, the experimental conditions needs optimized. The most important procedures will be described more in detail here:

**Safety measures**
A detailed risk assessment report has to be done before the experiments can be conducted. This has to identify the main risks in the experiments, and what measures has to be taken to prevent these from happening. It is important to always make sure that these safety measures have been done before the laser system is turned on. A detailed risk report has been added to the thesis and can be found in Appendix F. This will also describe procedures for a safe and correct start up of the laser system

**Alignment of camera**
To align the camera start taking a picture, and making sure that it captures the wanted target area. By mounting a laser on top of the camera, as seen in figure G.1, the camera angle can easily be checked. The laser-beam will reflect on the glass, and hit a specific area on the laser when the angle of the camera was right. If this happens the camera angle can be assumed to be normal to the plexiglass.

Being able to recreate the experiments, is also important. Noting the hight of the camera and the distance from test rig, enables future experiments to be conducted with the same distance, height and angle.

**Alignment of laser**
By hanging two threads from different bolts on the test rig seen in fig G.1 the angle of the laser could be corrected. By making the laser beam hit both of the threads, we could make sure that the laser hit the plexiglass straight on. This

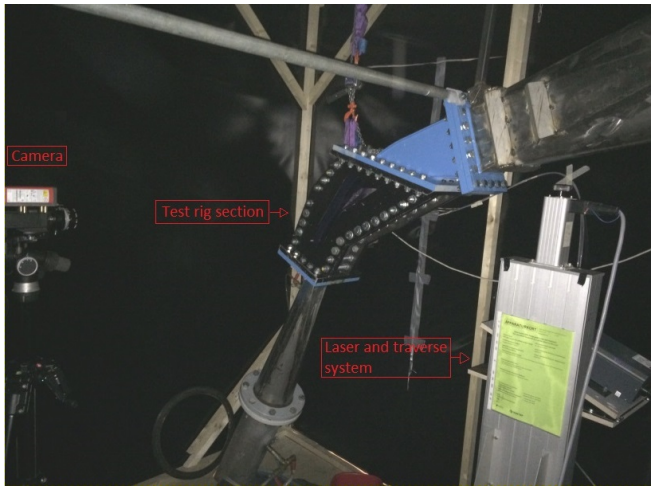


Figure G.1: Test rig and PIV system setup

ensures that the calibrated image plane is the same as the actual laser plane

**Positioning of laser**
This procedure makes sure that the laser illuminates the wanted area in the test rig. By using a "traverse" and software from DynamicStudios, it is possible to change the position of the laser. This ensures a optimized lit area.

After capturing images with the PIV system, it is also important to optimize the PIV conditions. This is done by checking the different rules described in chapter F.3. These procedures are here described in more practical detail:

**Laser energy**
To ensure that all off the particles are visible in the images it is important to use the maximum laser power(10 mJ). This will make the particles scatter as much as possible light and increase the chance of the software "catching" its position.

**Image capturing time**
To ensure that the maximum and minimum displacement, both within and out of plane is fulfilled, it is possible to change the capture time off the images $\Delta t$. By studying the particle movement and evaluating if the movement is too large, you have to decrease $\Delta t$, if it is too small, you have to increase it.

**Number of particles**
It is important to count the number of particles in each interrogation area to check if there is enough particles. To insert more particles, there was installed a pipe valve under the test section. By running the rig and creating low pressure in the test section, it is possible to insert a particle-water mix in to the closed system.

## G.2 PIV post processing

Before starting to use the software for vector field calculation, DynamcStudios has got many tools to pre analyse the captured images. These tools will make it easier for the software to later produce realistic velocity plots. The following methods was used to optimize the the described experiment results:

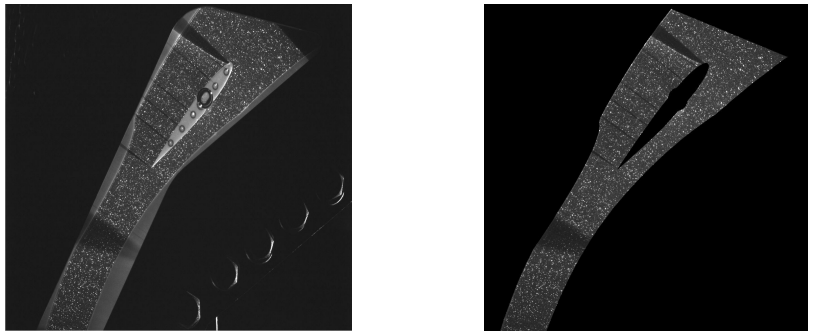

(a) Captured image before masking (b) Captured image after applied masking

Figure G.2: Image masking

**Image Masking**
This method is used to remove data in regions that are without interest in the experiments. This is done by defining a mask through marking the geometry outside the area of interest. By applying the mask to the captured images, the software will only analyse the flow region of the test rig.

**Image Min/Max**
After applying masking to the image, we continue to analyse the pictures. Image Min/Max is a method made to compute the power mean grey scale values from all the images taken. In more practical terms, the method creates an image of the common background in all of the acquired images, as shown in figure G.3a.

**Image Arithmetic**
Image arithmetic is a method that enables arithmetic on pixel values in two identically sized images. There are four types of operations that can be performed, these are subtraction, addition, division and multiplication.

By using the image arithmetic method, it is possible to subtract the e.g. the background(Image Min/Max) from the images with the particles G.2b. This will result in a clearer picture with only the particles left as seen in figure G.3b

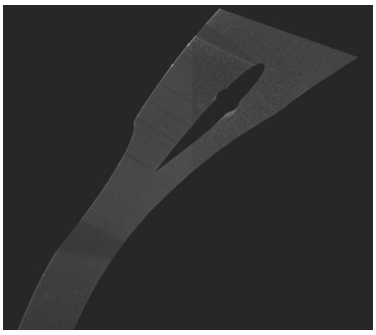

(a) Common background of acquired images

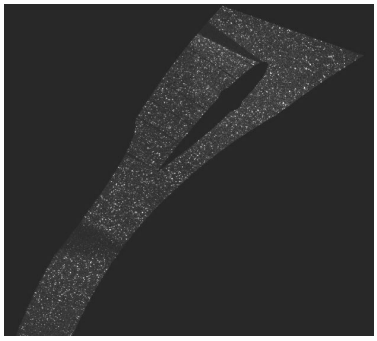

(b) Image Arithmetic

Figure G.3: Captured image with background subtracted

## G.3 Vector field calculation

**Cross-Correlation**
The Cross-Correlation method should be used after applying different image analysis methods to the captured images. Cross-Correlation will then track the particle motion and create the velocity vectors in a vector plot. As seen in figure G.4a, the Cross-Correlation analysis produces several "bad" vectors. To replace these with more realistic vectors, it is possible to apply additional methods of analysis:

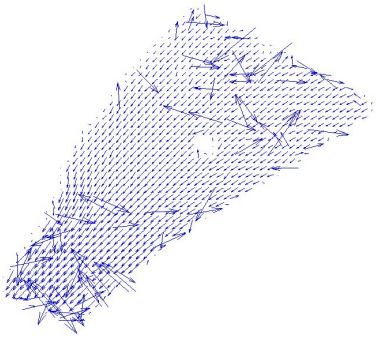

(a) Cross-Correlation analysis

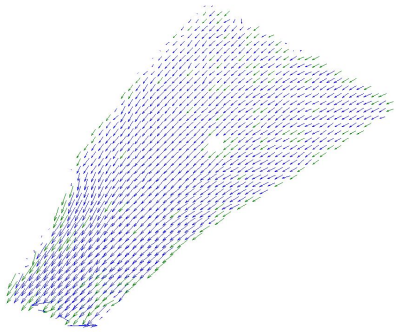

(b) Universal Outlier Detection

Figure G.4

**Universal Outlier Detection**
This is a analysis method used to detect and replace "bad" vectors. The substitution will be done with a normalized median test, using neighbouring vectors. How many of the neighbouring vectors that is used depends on the placement of the bad vector as shown in figure G.4b. The resulting vector plot, after applying

this method to the standard cross correlation PIV output, can be seen in figure G.4b.

**Moving Average Validation**
This is another analysis method used to validate vector maps. This is done by comparing each single vector, with the average of other vectors in a defined neighbourhood. If the deviation from the average is too big, it will be replaced with the average of the neighbours.

With the PIV software, the user can control parameters as the averaging area, the acceptance factor($A_p$) and number of iterations(n). The acceptance factor is used to determine if a vector should be replaced by the averaged vector. The new vector that replaces the bad vector will be calculated by interpolations, using n iterations.

**Vector Masking**
By applying the previously defined image mask to the calculated vector plots, it is possible to identify possible vectors that are outside the "interest area" defined by the image mask. These vectors are often a result of the previous methods that gives empty interrogation areas a interpolated value from the neighbours.

**Vector Statistics**
This is a method that calculates statistics from all of the calculated vector maps from the different captured images. The method creates a single vector map, with the mean velocity, the standard deviation and variance in each interrogation cell.